CrossMark

RESEARCH PAPER

A porous media finite element approach for soil instability including the second-order work criterion

Evanthia Kakogiannou[1] · Lorenzo Sanavia[1] · François Nicot[2] · Felix Darve[3] · Bernhard A. Schrefler[1]

Abstract This paper deals with the hydromechanical modelling of the initiation of failure in soils with particular reference to landslides. To this end, localized and diffused failure modes are simulated with a finite element model for coupled elasto-plastic variably saturated porous geomaterials, in which the material point instability is detected with the second-order work criterion based on Hill's sufficient condition of stability. Three different expressions of the criterion are presented, in which the second-order work is expressed in terms of generalized effective stress, of total stress and thirdly by taking into account the hydraulic energy contribution for partially saturated materials. The above-mentioned computational framework has been applied to study two initial boundary value problems: shear failure of a plane strain compression test of globally undrained water-saturated dense sand (where cavitation occurs at strain localization) and isochoric grain matter, and the onset of a flowslide from southern Italy due to rainfall (Sarno-Quindici events, May 5–6 1998). It is shown that the second-order work criterion applied at the material point level detects the local material instability and gives a good spatial indication of the extent of the potentially unstable domains in both the localized and diffused failure mechanisms of the cases analyzed, is able to capture the instability induced by cavitation of the liquid water and gives results according to the time evolution of plastic strains and displacement rate.

Keywords Cavitation · Elasto-plasticity · Finite element simulation · Landslides · Material instability · Multiphase porous media · Second-order work criterion

1 Introduction

Landslides are often triggered by rainfall. On the one hand, soil slopes can respond slowly to rainfall and move at very low speeds, but they can dominate sediment yields and landscape change for years or even millennia [45]. Slow-moving landslides typically involve thick, relatively fine-grained soils that yield large slip surface [21]. On the other hand, due to the usual large extension of rainfall events, hydrologically driven instability can be triggered over large areas and frequently involves shallow soil deposit of different grading and origin [10]. A diffuse, flow type of failure usually results from shallow slips [22]. Shallow, rapid landslides often involve thin, sandy soils on steep slopes; in this case, slope failure occurs abruptly with rapid post-failure acceleration [21]. Considering the destructiveness of this type of landslides, the understanding and the hydromechanical modelling of the mechanisms occurring inside the source areas are fundamental issues for the mitigation of the posed risk to life and facilities.

This paper focuses on hydromechanical conditions governing the initiation of failure in geomaterials and more in particular the onset of landslides in variably saturated slopes.

There are two rising questions when dealing with this matter: The first one concerns which approach to follow for the numerical modelling of rainfall-induced landslides in

✉ Lorenzo Sanavia
lorenzo.sanavia@unipd.it

1 Dipartimento di Ingegneria Civile, Edile e Ambientale, Università degli Studi di Padova, Padova, Italy

2 IRSTEA - Geomechanics Group, Grenoble, France

3 Laboratoire Sols Solides Structures, UJF-INPG-CNRS, Grenoble, France

order to predict the most realistic location and time of the failure occurrence. The most common approach for the numerical modelling of slope failure in engineering practice is to uncouple the fluid flow and slope stability problems and treat them in a sequential fashion. In this sense, a seepage analysis is performed first (assuming a rigid solid skeleton) for the calculation of the water pressure distribution, which is then followed by a limit equilibrium analysis for the slope stability problem, as, for example, in [8]. However, the behavior of a soil slope under rainfall conditions is fully coupled and closely related not only to the distribution of pore water pressure but also to the stress state during infiltration. Pore water pressure changes due to rainfall infiltration and seepage and will lead to changes in stress and consecutively deformation of the soil. In reverse, stress changes will modify the seepage process, because soil properties such as porosity, permeability and water storage capacity are affected by the changes in stress. Therefore, the seepage and stress–strain analysis have to be coupled and strongly linked to unsaturated conditions under rainfall (e.g., [3, 46]).

More exact solutions to the coupled hydromechanical analysis are obtained when the soils in the slope are considered deformable in variably saturated conditions. For this reason, in this work the modelling of rainfall-induced landslides is considered as a coupled variably saturated hydromechanical problem. For the numerical simulations, the geometrically linear finite element code Comes-Geo developed at the University of Padova, Italy, is used, in which soils are considered as non-isothermal elasto-plastic multiphase solid porous materials as developed in [37, 39, 40] following the works of [26] and [17–19].

The second matter, which is addressed in this paper, is the concept of material instability in multiphase geomaterials. As it is well known, slope failure is the ultimate outcome of instability mechanisms acting within the soil strata. These mechanisms can lead to a localized or diffuse mode of failure. In fact, these are the two main types of failure attributed to shallow rainfall-induced landslides: the shear failure, meaning the formation of shear bands due to strain localization which cause soil slips, and flowslide (related sometimes to static liquefaction processes), with no shear band formation resulting in flow-type failures [31].

Although the first type of failure can be described using localization theory, diffuse failure mode cannot be described either by classical empirical methods or by plasticity theories [27]. Therefore, there is the need for a more generalized criterion to be used which will be able to capture the instability independently of the failure mode. To this end, the second-order work criterion, based on Hill's sufficient condition of stability in elasto-plastic solids [20], has been applied for multiphase porous elasto-plastic solids and is

being examined in this paper to study the stability of initial boundary value problems. It consists in computing the sign of the second-order work for each material point of the domain, enabling to judge the potential instability of a spatial domain in which a set of local negative values occur and giving information for the detection of the onset of the failure. The argument for that is that the second-order work criterion is considered as a more generalized criterion since it has been proved mathematically that it is the first bifurcation criterion to be reached along a loading path [23] with respect to failure by divergence instabilities. What has been proved to be mathematically valid is being tested also numerically hereafter, on two different cases of multiphase finite element analyses.

In the following, the mathematical model for non-isothermal multiphase porous materials is summarized first. Subsequently, the definition of the second-order work criterion is reviewed and three different expressions are presented which could be used in the case of variably saturated porous materials; the second-order work is expressed in terms of generalized effective stress, of total stress and thirdly by taking into account the hydraulic energy contribution for the case of partially saturated soils. Finally, the numerical results of two multiphase finite element analyses are presented and discussed: Shear failure is being studied through an example of a finite element analysis of a plane strain compression test on globally undrained water-saturated dense and isochoric sand [39], followed then by the finite element analysis of a real case study from southern Italy (Sarno-Quindici flowslide events due to rainfall, May 5–6 1998).

2 Mathematical model

The mathematical model necessary to simulate the thermo-hydromechanical transient behavior of fully and partially saturated elasto-plastic porous media is developed in [39] following the works by Lewis and Schrefler [26] and [42] and using averaging theories by Hassanizadeh and Gray [17–19]. For sake of brevity, only a summary of the underlying physical model is presented here. For the complete description of the model from its mathematical formulation to the numerical implementation, the reader can refer to the above-mentioned works of the authors.

The geomaterial is considered as a variably saturated porous medium and is treated as a multiphase system composed of a solid skeleton (s) with open pores filled with liquid water (w) and gas (g). All constituents are assumed to be immiscible and chemically non-reacting, except for the gas which is assumed to behave as an ideal mixture of dry air (non-condensable gas, ga) and water vapor (condensable one, gw).

At the microscopic level, the solid constituents and the liquid water are considered incompressible, while the gas is compressible. At the macroscopic level, the porous material is modelled by a substitute continuum that simultaneously fills the entire domain, instead of the real fluids and the solid which fill only a part of it. In this substitute continuum, each constituent π has a reduced density, which is obtained through the volume fraction $\eta^\pi(\mathbf{x}, t) = dv^\pi(\mathbf{x}, t)/dv(\mathbf{x}, t)$, where dv is the volume of the average volume element (representative elementary volume, REV) of the porous medium and dv^π is the volume occupied by the constituent π in dv. $\mathbf{x}$ is the vector of the spatial coordinates and t the current time.

The following assumptions are made additionally, in the mathematical model [26]: all fluids are in contact with the solid phase, and the solid is deformable resulting in coupling of the fluid, the solid and the thermal effects. The constituents are isotropic, homogeneous and microscopically non-polar. Local thermal equilibrium among the solid, gas and liquid phases is assumed. In the model, heat conduction, heat convection, vapor diffusion, liquid water flow due to pressure gradients or capillary effects and water phase change (evaporation and condensation) inside the pores are taken into account.

2.1 Macroscopic balance equations

The final model consists of four balance equations: mass balance of the dry air, mass balance of the water species (both liquid and vapor phase change is taken into account), enthalpy of the whole medium (latent heat of the phase change is considered) and the equilibrium equations of the multiphase medium.

They are completed with an appropriate set of constitutive and state equations, as well as some thermodynamic relationships.

The governing equations of the model are expressed in terms of the chosen state variables: gas pressure $p^g(\mathbf{x}, t)$, capillary pressure $p^c = [p^g - p^w]$ [16] where $p^w(\mathbf{x}, t)$ is the liquid water pressure, temperature $T(\mathbf{x}, t)$ and the displacement vector of the solid matrix $\mathbf{u}(\mathbf{x}, t)$. Pore pressure is defined as compressive positive for the fluids, while stress in the solid phase is defined as tension positive. The macroscopic equations of the model are now summarized [15, 26].

The equilibrium equation of the mixture in terms of generalized Cauchy effective stress $\sigma'(\mathbf{x}, t)$ [41] assumes the form:

$$div(\boldsymbol{\sigma}' - [p^g - S^w p^c]\mathbf{1}) + \rho\mathbf{g} = \mathbf{0} \tag{1}$$

where $\rho(\mathbf{x}, t)$ is the density of the mixture, $\rho = [1 - n]\rho^s + nS_w\rho^w + nS_g\rho^g$ with $n(\mathbf{x}, t) = 1 - \eta^s$ is the porosity, $S_w(\mathbf{x}, t)$ and $S_g(\mathbf{x}, t)$ are the liquid water and gas degree of saturation, respectively $(S_w + S_g = 1;\quad \eta^w = nS_w;\ \eta^g = nS_g)$. ρ^π is the microscopic or bulk mass density with $(\pi = s, w, g)$, $\mathbf{g}$ is the gravity acceleration vector and $\mathbf{1}$ is the second order identity tensor.

The mass balance equation for the solid phase, the liquid water and the water vapor is:

$$n[\rho^w - \rho^{gw}]\left[\frac{\partial S_w}{\partial t}\right] + [\rho^w S_w - \rho^{gw}[1 - S_w]]div\left(\frac{\partial \mathbf{u}}{\partial t}\right)$$
$$+ [1 - S_w]n\frac{\partial \rho^{gw}}{\partial t} - div\left(\rho^g \frac{M_\alpha M_w}{M_g^2}\mathbf{D}_g^{gw}grad\left(\frac{\partial p^{gw}}{\partial p^g}\right)\right)$$
$$+ div\left(\rho^w \frac{\mathbf{k}k^{rw}}{\mu^w}[-grad(p^g) + grad(p^c) + \rho^w\mathbf{g}]\right)$$
$$+ div\left(\rho^{gw} \frac{\mathbf{k}k^{rg}}{\mu^g}[-grad(p^g) + \rho^w\mathbf{g}]\right) - \beta_{swg}\frac{\partial T}{\partial t} = 0 \tag{2}$$

where $\rho^{gw}(\mathbf{x}, t)$ is the microscopic mass density of the water vapor and $\mathbf{k}(\mathbf{x}, t) = \mathbf{K}_w\mu^w/(\rho^w g)$ is the intrinsic permeability tensor of the porous matrix in saturated condition (m^2), with $\mathbf{K}_w(\mathbf{x}, t)$ the hydraulic conductivity tensor (m/s). $k^{rw}(\mathbf{x}, t)$ is the water relative permeability parameter and $\mu^w(\mathbf{x}, t)$ the dynamic viscosity of liquid water, function of the temperature $T(\mathbf{x}, t)$. Similarly, $k^{rg}(\mathbf{x}, t)$ is the gas relative permeability parameter and $\mu^g(\mathbf{x}, t)$ the dynamic viscosity of gas; $\beta_{swg}(\mathbf{x}, t) = \beta_s[1 - n][S_g\rho^{gw} + S_w\rho^w]$, where $\beta_s(\mathbf{x}, t)$ is the solid cubic thermal expansion coefficient; $\mathbf{D}_g^{gw}(\mathbf{x})$ is the effective diffusivity tensor of water vapor (the diffusing phase) in the gas phase (the phase in which diffusion takes place) contained in the pore space, function of the tortuosity factor, and M_a, M_w and $M_g(\mathbf{x}, t)$ are the molar mass of dry air, liquid water and gas mixture, respectively. In order to account for the diffusive–dispersive flux of the vapor in the gas phase, Fick's law is used, while the advective flows are modelled with Darcy's law.

The mass balance equation for dry air is:

$$n\rho^{g\alpha}\left[\frac{\partial S_w}{\partial t}\right] + \rho^{g\alpha}[1 - S_w]div\left(\frac{\partial \mathbf{u}}{\partial t}\right)$$
$$+ nS_g\frac{\partial \rho^{g\alpha}}{\partial t} - div\left(\rho^g \frac{M_\alpha M_w}{M_g^2}\mathbf{D}_g^{g\alpha}grad\left(\frac{\partial p^{g\alpha}}{\partial p^g}\right)\right)$$
$$+ div\left(\rho^{g\alpha} \frac{\mathbf{k}k^{rg}}{\mu^g}[-grad(p^g) + \rho^g\mathbf{g}]\right)$$
$$- \beta_{swg}\rho^{g\alpha}[1 - n][1 - S_w]\frac{\partial T}{\partial t} = 0 \tag{3}$$

where, similarly, $\rho^{ga}(\mathbf{x}, t)$ is the microscopic mass density of the dry air and $\mathbf{D}_g^{ga}(\mathbf{x})$ is the effective diffusivity tensor of dry air in the gas phase contained in the pore space. Equations (2) and (3) include the mass balance equation for the solid phase:

$$\frac{\partial n}{\partial t} = [1 - n]\mathrm{div}\left(\frac{\partial u}{\partial t}\right) - [1 - n]\beta_s \frac{\partial T}{\partial t} \tag{4}$$

The enthalpy balance equation of the mixture is:

$$\left(\rho C_p\right)_{\mathrm{eff}} \frac{\partial T}{\partial t} + \rho^w C_p^w \left(\frac{\mathbf{k}k^{rw}}{\mu^w}[-\mathrm{grad}(p^g) + \mathrm{grad}(p^c) + \rho^w \mathbf{g}]\right) \cdot \mathrm{grad}(T)$$
$$+ \rho^g C_p^g \left(\frac{\mathbf{k}k^{rg}}{\mu^g}[-\mathrm{grad}(p^g) + \rho^g \mathbf{g}]\right) \cdot \mathrm{grad}(T)$$
$$- \mathrm{div}(\chi_{\mathrm{eff}} \mathrm{grad}(T)) = -\dot{m}_{\mathrm{vap}}\Delta H_{\mathrm{vap}} \tag{5}$$

where $\left(\rho C_p\right)_{\mathrm{eff}}$ is the effective thermal capacity of the porous medium, $\rho^w C_p^w$ and $\rho^g C_p^g$ are the specific heat of the water and gas mixture, respectively, χ_{eff} is the effective thermal conductivity of the porous medium, and the right-hand side term considers the contribution of the evaporation and condensation. This balance equation takes into account the heat transfer through conduction and convection as well as latent heat transfer and neglects the terms related to the mechanical work induced by density variations due to temperature changes of the phases and induced by volume fraction changes [26].

2.2 Constitutive relations

For the gaseous mixture which is assumed to be a perfect mixture of two ideal gases (dry air and water vapor), the ideal gas law is introduced. The equation of state of perfect gas (the Clapeyron equation) and Dalton's law are applied to dry air (ga), water vapor (gw) and moist air (g). In the partially saturated zones, the water vapor pressure $p^{gw}(\mathbf{x}, t)$ is obtained from the Kelvin–Laplace equation:

$$p^{gw} = p^{gws}(T)\exp\left(-\frac{p^c M_w}{\rho^w RT}\right) \tag{6}$$

where the water saturation vapor pressure $p^{gws}(\mathbf{x}, t)$ depending only from the temperature T can be calculated from the Clausius–Clapeyron equation or from an empirical equation. The saturation $S_\pi(\mathbf{x}, t)$ and the relative permeability $k^{r\pi}(\mathbf{x}, t)$ are experimentally determined functions of the capillary pressure $p^c(\mathbf{x}, t)$ and the temperature $T(\mathbf{x}, t)$:

$$S_\pi = S_\pi(p^c, T), \quad k^{r\pi} = k^{r\pi}(p^c, T), \quad \pi = w, g \tag{7}$$

The mechanical behavior of the soil skeleton is described within the classical rate-independent elasto-plasticity theory for geometrically linear problems. The yield function $F(\mathbf{x}, t)$ restricting the effective stress state is assumed in the form of the Drucker–Prager yield surface with isotropic linear hardening/softening behavior and non-

associated plastic flow as developed in [39] and is used here for the sake of simplicity:

$$F(p', \mathbf{s}', \xi) = 3\alpha_F p' + \|\mathbf{s}'\| - \beta_F \sqrt{\frac{2}{3}}[c + h\xi] \tag{8}$$

in which $p' = \frac{1}{3}[\sigma' : \mathbf{1}]$ is the mean effective Cauchy stress, $\|\mathbf{s}'\|$ is the L_2 norm of the deviator effective Cauchy stress tensor $\sigma'(\mathbf{x}, t)$, $c(\mathbf{x}, t)$ is the soil cohesion, sum of the effective cohesion $c'(\mathbf{x})$ in water-saturated conditions and the apparent cohesion $p^c \tan \varphi^b$ (where $\varphi^b(\mathbf{x})$ is the internal soil friction angle associated with the capillary pressure), linked through the relation: $c = c' + p^c \tan \varphi^b$ [14]. $\alpha_F(\mathbf{x})$ and $\beta_F(\mathbf{x})$ are two material parameters related to the internal friction angle $\varphi(\mathbf{x})$ of the soil

$$\alpha_F = 2\frac{\sqrt{\frac{2}{3}}\sin\varphi}{3 - \sin\varphi}, \quad \beta_F = 2\frac{6\cos\varphi}{3 - \sin\varphi} \tag{9}$$

and $h(\mathbf{x})$ and $\xi(\mathbf{x}, t)$ are the hardening/softening modulus and the equivalent plastic strain variable, respectively. The expression of the potential surface $Q(\mathbf{x}, t)$ is defined in [38]; it is similar to Eq. (8), with the parameters α and β dependent on the dilatant angle instead of the angle of internal friction used in Eq. (9). The return mapping algorithm and the consistent tangent operator for the singular behavior of the Drucker–Prager yield surface in the apex zone are developed in [39] following [38] using the concept of multi-surface plasticity.

2.3 Initial and boundary conditions

For the model closure, the initial and boundary conditions are presented according to [39, 40]. The initial conditions specify the full fields of the primary state variables at the reference time $t = t_0$, on the whole domain and on its boundaries as:

$$p^g = p_0^g, \ p^c = p_0^c, \ T = T_0, \mathbf{u} = \mathbf{u}_0 \text{ on } B \cup \partial B \tag{10}$$

The boundary conditions can be of the first kind (Dirichlet's boundary conditions) prescribing the values of the primary variables on ∂B_π for $t \geq t_0$:

$$p^g = \hat{p}^g \quad \text{on} \quad \partial B_g, \quad p^c = \hat{p}^c \quad \text{on} \quad \partial B_c$$
$$T = \hat{T} \quad \text{on} \quad \partial B_T, \quad \mathbf{u} = \hat{\mathbf{u}} \quad \text{on} \quad \partial B_u \tag{11}$$

or of the third type (Cauchy's type) prescribing the value of the outward normal fluxes (including the convective fluxes) on ∂B_π^q:

$$\left(nS_g\rho^{ga}\mathbf{v}^{gs} + J_d^{gw}\right) \cdot \mathbf{n} = q^{ga} \quad \text{on} \quad \partial B_g^q$$
$$\left(nS_w\rho^w\mathbf{v}^{ws} + nS_g\rho^{gw}\mathbf{v}^{gs} + J_d^{gw}\right) \cdot \mathbf{n} = q^{gw} + q^w$$
$$\quad + \beta_c\left(\rho^{gw} - \rho_\infty^{gw}\right) \text{ on } \partial B_c^q$$
$$\left(nS_w\rho^w\mathbf{v}^{ws}\Delta H_{vap} - \chi_{\text{eff}}\,\text{grad}\,T\right) \cdot \mathbf{n} = q^T + \alpha^c(T - T_\infty)$$
$$\quad + e\sigma_0\left(T^4 - T_\infty^4\right) \text{ on } \partial B_c^q$$
$$\boldsymbol{\sigma} \cdot \mathbf{n} = \mathbf{t} \quad \text{on} \quad \partial B_u^q$$

$$(12)$$

where $\mathbf{n}(\mathbf{x}, t)$ is the unit normal vector, pointing toward the surrounding gas, and $q^{ga}(\mathbf{x}, t)$, $q^{gw}(\mathbf{x}, t)$, $q^w(\mathbf{x}, t)$, $q^T(\mathbf{x}, t)$ are, respectively, the imposed fluxes of dry air, water vapor, liquid water and the imposed heat flux, $\mathbf{t}(\mathbf{x}, t)$ is the imposed traction vector related to the total Cauchy stress tensor $\boldsymbol{\sigma}(\mathbf{x}, t)$, $\rho_\infty^{gw}(\mathbf{x})$ and $T_\infty(\mathbf{x})$ are the mass concentration of water vapor and the temperature in the far field of undisturbed gas phase, $e(\mathbf{x})$ is the emissivity of the interface, σ_0 is the Stefan–Boltzmann constant, while $\alpha_c(\mathbf{x})$ and $\beta_c(\mathbf{x})$ are the convective heat and mass exchange coefficients, respectively.

3 Finite element formulation

The governing equations of the problem are discretized in space by means of the finite element method. Their discretized form is obtained by means of the Bubnov–Galerkin method for the discretization in space. The time discretization is accomplished through a fully implicit finite difference scheme. Because of the nonlinearity of the system of equations, the solution is obtained with a Newton–Raphson type procedure. Monolithic approach is adopted because of the strong coupling of Eqs. (1)–(5). Details concerning the matrices and the residual vector of the linearized equations system of the finite element model can be found in [39].

4 Second-order work material instability criterion

Although the notion of failure in soils (or more generally geomaterials) was long described as a perfect plastic limit, it has been observed in practice that failure can occur well before the Mohr–Coulomb criterion is met. This is due to the non-associated behavior (the yield surface does not coincide with the plastic potential, which leads to a non-symmetric constitutive tensor) of cohesive and/or frictional materials, such as soils. According to [12, 23] in case of such materials, one can find an unstable domain strictly inside the plastic limit envelope. What is more, material instabilities can lead to diffuse modes of failure inside the plastic limit condition, which are characterized by the lack of localization patterns, and for this reason, it cannot be detected neither by a plastic limit criterion nor by a localization criterion [13, 33]. A characteristic example of this kind of failure can be illustrated through an undrained triaxial test on loose sand. If a small additional force is applied at the stress peak value, a sudden failure occurs with no localization pattern strictly inside the Mohr–Coulomb plastic limit condition (Fig. 1).

Therefore, a need is motivated for a more generalized criterion of instability. Within this context, we examine the concept of the second-order work which was proposed by Hill [20]. Hill connected the notion of stability with the expression of the second-order work. At the material point level, it is described as follows: A mechanical stress–strain state is considered as stable if the second-order work is strictly positive for any couple $(d\boldsymbol{\sigma}, d\boldsymbol{\varepsilon})$ linked by the rate-independent constitutive relation:

$$\forall (d\boldsymbol{\sigma}, d\boldsymbol{\varepsilon}) \in \mathbb{R}^{2n}\backslash\{0\} \quad \text{with} \quad d\boldsymbol{\varepsilon} = \mathbf{M} : d\boldsymbol{\sigma},$$
$$W_2 = d\boldsymbol{\sigma} : d\boldsymbol{\varepsilon} > 0$$

$$(13)$$

where n is the dimension of the stress (or strain $\boldsymbol{\varepsilon}$) space and $\mathbf{M}$ is the stiffness tensor.

Different interpretations of this criterion have been provided by considerable amount of studies with the aim to give to it an additional physical meaning. These studies have led to the notions of controllability and sustainability. The controllability notion, which was introduced by Nova [34], related Hill's criterion to the boundary and loading conditions (control conditions) imposed on a porous solid. Loss of controllability of a certain loading path can be described as loss of uniqueness of the incremental solution.
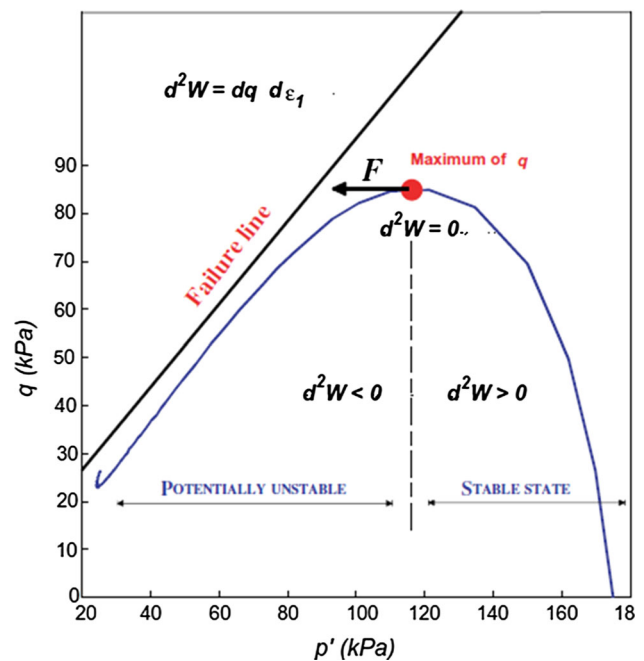

Fig. 1 CIU stress path of saturated, loose sand [13]

The notion of sustainability was introduced by Nicot [30, 32] and relates the second-order work criterion to the transition from a stationary regime to a dynamic one, without any external input and accompanied with a burst of kinetic energy. Loss of sustainability is connected to failure.

Based on the above concepts, the vanishing of the value of the second-order work indicates potential instability. It can then be considered as a generalized criterion because, in case of non-associated materials, the second-order work W_2 (which first vanishes together with the determinant of the symmetric part of the stiffness tensor $\mathbf{M}$, [27]) becomes zero before the vanishing of the determinant of the constitutive tensor $\mathbf{M}$ and of the determinant of the acoustic tensor [11, 23, 27].

Following this choice of using the second-order work criterion (instead of the study of bifurcation at constitutive level), there is still an open question regarding the type of stress that should be used in Eq. (13) when studying the stability of a multiphase porous body. There is the debate on using effective or total stress; furthermore, in the case of a partially saturated medium, the hydraulic contribution for the stability of the porous body can be raised. In fact, the stability of a material specimen is related to the skeleton stability. The specimen collapses if the skeleton collapses. However, the skeleton stability depends on the pore pressures applied to the particles. The fluid phases are therefore involved in the specimen stability, similarly to the so-called weak phases, surrounding force chains, which actively participate in the strength of a dry granular specimen [43]. Discussing which stress expression should be used is not the objective of the manuscript. Thus, three different expressions are presented hereafter for the second-order work, which could be used in the case of variably saturated porous materials.

Firstly, it is written in terms of effective stress, $W_2(\mathbf{x}, t)$

$$W_2 = d\boldsymbol{\sigma}' : d\boldsymbol{\varepsilon} \qquad (14)$$

where $\sigma'(\mathbf{x}, t)$ is the generalized Cauchy effective stress [41], as it seems to be the most natural choice when modelling variably saturated geomaterials.

Subsequently, the second-order work is expressed in terms of total stress, $W_{2_{tot}}(\mathbf{x}, t)$:

$$\begin{aligned} W_{2_{tot}} &= d\boldsymbol{\sigma} : d\boldsymbol{\varepsilon} = d(\boldsymbol{\sigma}' - [p^g - S_w p^c]\mathbf{1}) : \\ d\boldsymbol{\varepsilon} &= d\boldsymbol{\sigma}' : d\boldsymbol{\varepsilon} + d(S_w p^c)d\varepsilon_v - dp^g d\varepsilon_v \\ &= W_2 + d(S_w p^c)d\varepsilon_v - dp^g d\varepsilon_v \end{aligned} \qquad (15)$$

as the total energy of a porous system, from which the second-order work criterion is derived, involves total stress. Turning back to the physical origin of the second-order work, stemming from an energy conservation equation that embeds force balance, the total stress stands as the natural stress candidate.

Finally, the extended expression of the second-order work for the case of a partially saturated medium is presented, $W_{2_{unsat}}(\mathbf{x}, t)$, as it was proposed by [4]:

$$W_{2_{unsat}} = d\boldsymbol{\sigma}' : d\boldsymbol{\varepsilon} - ndp^c dS_w = W_2 - ndp^c dS_w \qquad (16)$$

In the numerical simulations that follow, the above expressions are implemented in the finite element code Comes-Geo [26, 37, 39, 40] to investigate the role of the second-order work criterion on the detection of the material point instability and the prediction of the failure mechanism in light of the three expressions (14)–(16). To this end, the second-order work, $W_{2_{tot}}$, Eq. (15), and $W_{2_{unsat}}$, Eq. (16), has been also written substituting the term $d\boldsymbol{\sigma}' : d\boldsymbol{\varepsilon}$ with W_2 from Eq. (14).

The three expressions above are implemented in their discrete form within the incremental approach used in the finite element method for nonlinear problems, i.e., substituting the differential quantity $d\square$ with its discrete counterpart $\Delta\square = \square_{n+1} - \square_n$, where $n + 1$ is the current time step and n is the previous time step. Their numerical values will then be plotted in both the space and time domains, and the results will be analyzed in Sects. 5 and 6 for the two initial boundary value problems considered in this work. It is worth mentioning that this computation does not affect the results, as it is just a post-processing of variables computed by the finite element algorithm.

5 Finite element analysis of a globally undrained dense sand sample

In this section, a simulation of rapid desaturation (due to cavitation) of an initially water-saturated porous media is analyzed with the finite element code Comes-Geo [26, 37, 39, 40]. The example was previously solved by [39] and re-analyzed here. It is inspired by the globally undrained plane strain biaxial compression test on water-saturated dense sands where strain localization and cavitation of the pore water (change of the liquid phase to vapor) were experimentally observed [29]. The original contribution in this section is the use of the second-order work criterion to detect the unstable material points of the domain and the prediction of the failure mechanism.

A rectangular sample of homogeneous soil (Hostun dense sand) of 34 cm height and 10 cm width (Fig. 2) has been discretized using a regular grid of 340 biquadratic isoparametric finite elements (with the dimension of the finite elements similar to that of the experimental shear band, to fix the width of the localized zones) with reduced Gaussian (2×2) integration scheme (widely used in localization analysis). The material is initially saturated with liquid water; hydrostatic distribution of water
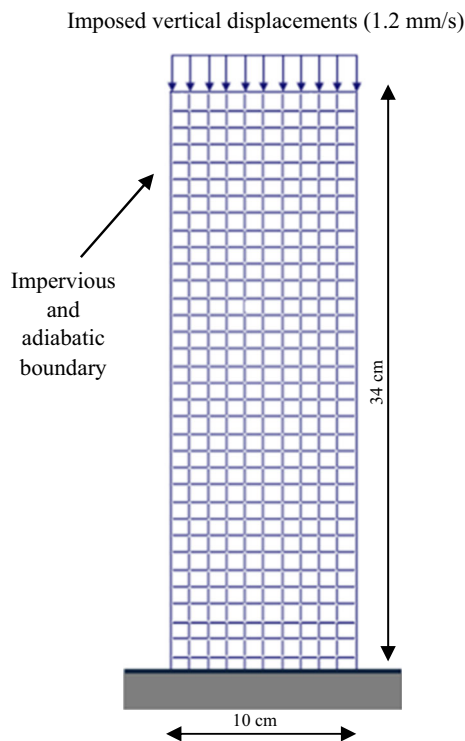
Imposed vertical displacements (1.2 mm/s)

Fig. 2 Description of the geometry, boundary and loading conditions

Table 1 Material parameters assumed for dense sand [39]

Definition	Label	Dense sand
Solid grain density	ρ^s (kg/m^3)	2000
Young's modulus	E (Pa)	3.0E + 07
Poisson's ratio	v (–)	0.4
Friction angle	φ (°)	30.0
Cohesion in water-saturated conditions	c (Pa)	5.0E + 05
Angle of dilatancy	ψ (°)	20
Softening modulus	h (Pa)	−1.0E + 06
Hydraulic conductivity	k (m/s)	5E−7
Initial porosity	n (–)	0.2

pressure, with the free surface located at the top of the specimen, and geostatic effective stress are assumed as initial conditions. These initial conditions are obtained in Comes-Geo computing the hydromechanical state in equilibrium with the given boundary conditions and the gravity loads.

The boundary of the sample is impervious and adiabatic. Imposed vertical displacements are applied on the top surface with the constant velocity of 1.2 mm/s until strain localization is observed. Vertical and horizontal displacements are constrained at the bottom surface. Plane strains and quasi-static loading conditions are assumed.

The initial temperature in the sample is constant and fixed at the ambient value (i.e., 20 °C). Gravity acceleration is taken into account during the computation (Eqs. 1–3, 5). The mechanical behavior of the solid skeleton is simulated using the elasto-plastic Drucker–Prager constitutive model with isotropic linear softening behavior and non-associated plastic flow. The material parameters used in the computation are listed in Table 1. In the analysis, the dilatant behavior of dense sands is simulated selecting a positive value of the angle of dilatancy ($\psi = 20°$).

The results of the simulation after 27 s of loading are presented. The accumulation of plastic strains can be observed in narrow zones (shear bands) where the contour of the equivalent plastic strain (i.e., the L2 norm of the plastic strain tensor) is depicted (Fig. 3a); it can be noted

that the shear bands are not centrally located in the specimen because they develop from the lower corners, which are the zones with higher stress concentration due to the initial geostatic stress, the vertical displacement load applied to the top surface and the constraints applied to the bottom surface [39]. Other two minor shear bands develop in the upper part of the specimen. The contour of the second-order work, W_2 (discretized Eq. 14), is presented in Fig. 3b, where only the nil and negative values are plotted. As can be observed, the unstable zones ($W_2 \leq 0$) are detected inside the shear bands. Subsequently, in Fig. 3c, the positive values of the volumetric strains, which are due to the dilatant behavior of the dense sand in plasticity, are plotted and it is observed that they are also detected within the shear bands where the equivalent plastic strains are accumulated. Consequently, pore water pressure decreases, up to the development of capillary pressure (Fig. 4a).

Subsequently, desaturation in the strain localization zones develops (Fig. 4b), as experimentally observed [29], due to the formation of a vapor phase as the water pressure decreases below the water saturation pressure ($p^{gws} = 2338.8$ Pa at $T = 20$ °C). This effect is captured by the model, because of the coupling between the thermo-hydro and mechanical parts, as it is shown in Fig. 4c, with the vapor phase appearing only inside the dilatant plastic zones.

Finally, the contour plot of the second-order work written in terms of effective stress, W_2 (Eq. 14; Fig. 3b), is compared with the contour of the second-order work written in terms of total stress, W_{2tot} (Eq. 15; Fig. 5a), and taking into account the hydraulic energy contribution, W_{2unsat}, (Eq. 16; Fig. 5b). The pattern of the shear band is quite well detected in all three cases, with similar lower values, even if it is observed that the whole shear band cannot be captured (see Fig. 3a). In the case of the expression W_2 in terms of effective stress, slightly more unstable points are detected and even lower values are reached according to the results.

Hereafter, the evolution of the second-order work W_2, of the water saturation degree, of the equivalent plastic strain,
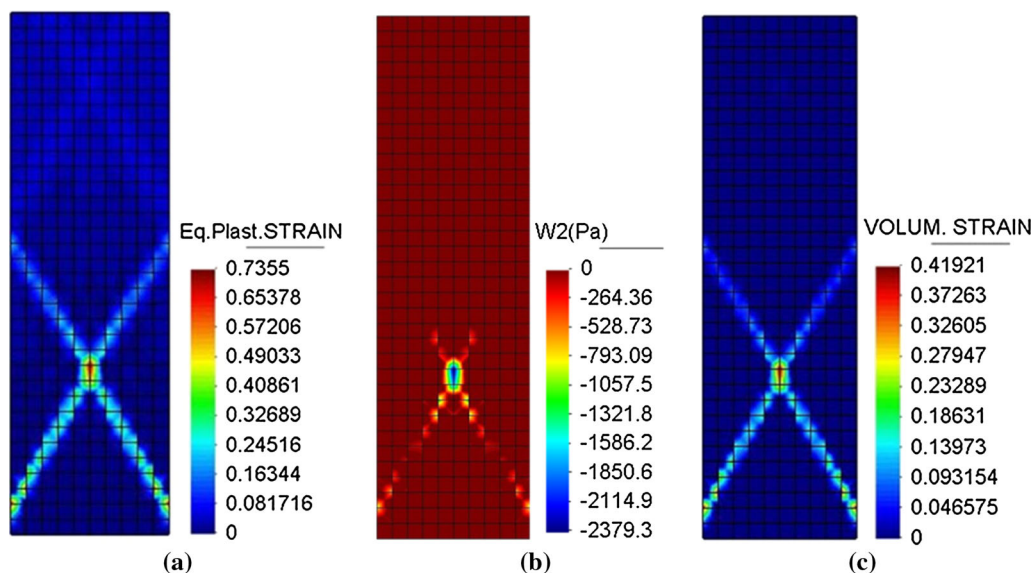
Fig. 3 Numerical results after 27 s of loading (values plotted at the Gauss points): **a** equivalent plastic strain contour (–); **b** negative values of the second-order work W_2 contour (Pa); **c** positive values of the volumetric strain contour (−)
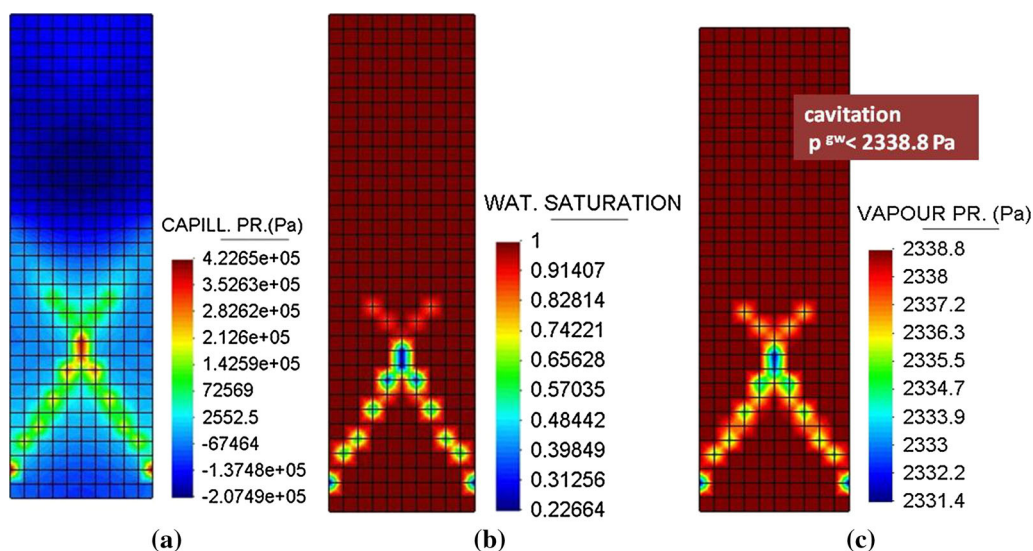

Fig. 4 Numerical results after 27 s of loading (values plotted at the nodal points): **a** capillary pressure contour (Pa); **b** water degree of saturation contour (–); **c** vapor pressure contour (Pa)

of the capillary pressure and of the volumetric strain is presented at the Gauss points of four different elements (Fig. 6): at the center of the specimen (element 105), near the base where the shear band initiates (element 20), in the elastic zone (element 27) and at the top of the shear band (element 162, where the minimum values of the equivalent plastic strain are depicted). The location of the Gauss points is shown in Fig. 6a, within the contour of equivalent plastic strain drawn in a lower part of the specimen.

It is observed that the evolution of the equivalent plastic strain starts after 7 s of loading (Fig. 6d) and, consequently,

the volumetric strain becomes positive due to the dilatant plastic behavior of the material (Fig. 6f). Negative value of the volumetric strain is observed only for the point in the elastic domain (element 27, Fig. 6f). At the same time, the capillary pressure starts to increase. Positive values for the capillary pressure greater than the air entry value (equal to 2.0 kPa), which correspond to desaturation, are only obtained later on at the material points of elements 20 and 105 located within the plastic zones which cavitates (Fig. 6e). For the same elements (105 and 20), the second-order work (in terms of effective stress, W_2) at the material
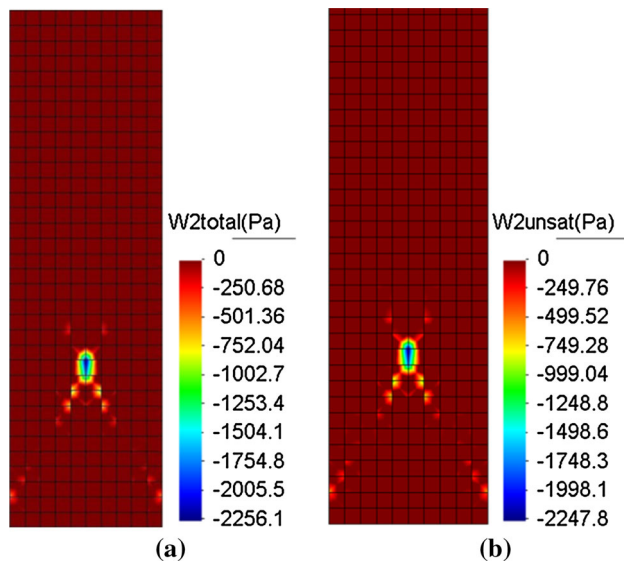
Fig. 5 Numerical results of the second-order work (Pa) after 27 s of loading (values plotted at the Gauss points): **a** in terms of total stress W_{2tot}; **b** expression for partially saturated soils W_{2unsat}

point level becomes negative, starting from 15 s as shown in Fig. 6b, after the development of a certain amount of plastic strain.

A comparison of the results obtained from the different expressions derived for the second-order work (Eqs. 14–16), at the material point of the element 105, is shown in Fig. 7a. As it can be seen, the results of the three expressions are quite similar. A closer look shows that the expression of the second-order work written in terms of effective stress (W_2) and the one accounting for the partially saturated conditions (W_{2unsat}) gives the same results until the point of desaturation (after 24 s of loading). After that point, W_{2unsat} gives slightly higher values. The second-order work in terms of total stress (W_{2tot}) becomes zero slightly after W_2 (at 17 s of loading) and obtains greater values comparing to the other two expressions.

What is more important is that the comparison with Fig. 6 identifies four zones: a first stable zone during the elastic behavior, a second zone in which the second-order work decreases down to negative values when plasticity occurs, a third zone in which the second work increases when capillary pressure develops up to cavitation and finally, a fourth zone in which the second work decreases rapidly because of cavitation.

The results of the three expressions are compared in Fig. 7b and c, where the difference of the W_{2unsat} and of the W_{2tot} relative to W_2 is plotted. The difference $W_{2unsat} - W_2$ (Fig. 7b) is slightly positive only after the moment of desaturation, showing that W_2 is slightly more negative than W_{2unsat} because the term $-ndp^c dS_w$ is always positive (or nil in water-saturated conditions, see Eq. 16). It

is observed that also the difference $W_{2tot} - W_2$ is positive (Fig. 7c), but the time histories of the two variables are quite similar. Then, Fig. 7d compares W_{2tot} with W_{2unsat} showing similar trends of Fig. 7c.

Finally, the von Mises constitutive model has been also tested on the same analysis. As this model is reduced from the Drucker–Prager one, Eq. (8), by setting the coefficients α_F and β_F to zero and one, respectively, and assuming associated plastic flow, the values of the elasto-plastic model parameters (Young's modulus, Poisson's ratio, initial yield and softening modulus) are those reported in Table 1. Also the values of the parameters for the porous material (solid grain density, hydraulic conductivity and porosity) are those of Table 1. In this case, it is observed that the second-order work W_2 captures the whole shear band (Fig. 8b) and that the equivalent plastic strain starts appearing at the same time step with the first negative value of the second-order work at the material point level (Fig. 8c). This is explained by the fact that von Mises plasticity considers associated plastic flow; in the case of associated plasticity, since the tangent stiffness matrix **M** of the solid is symmetric, the second-order work criterion (det $\mathbf{M}_s = 0$) will give the same results as the limit criterion (det $\mathbf{M} = 0$), [13].

In summary, the analysis of the strain localization test simulated in this section shows that the three expressions of the second-order work (Eqs. 14–16) give similar results in terms of spatial and temporal distribution, especially for W_2 and W_{2unsat}.

Moreover, the second-order work criterion is able to capture the instability induced by cavitation of the pore water. The comparison between the results obtained from the Drucker–Prager and the von Mises constitutive model evidences the role of the volumetric plasticity, which delays instability up to the development of a certain amount of plastic strains, because the first indication of instability (negative second-order work) is obtained later than the beginning of the plastic strains.

6 Finite element analysis of the Sarno flowslide

At the beginning of May 1998, landslides of the flow type occurred along the slopes of the Pizzo d'Alvano carbonate massif (Campania region, southern Italy) because of a severe rainfall event throughout the area [5, 9]. The case addressed in this section occurred on May 5, 1998, and constitutes one of these hundred slope instability events. In the sample area shown in Fig. 9, the section A–A has been analyzed which is of 400 m length, with a variable thickness between 2 and 5 m and composed of 3 types of materials: upper ashy, pumice and lower ashy.
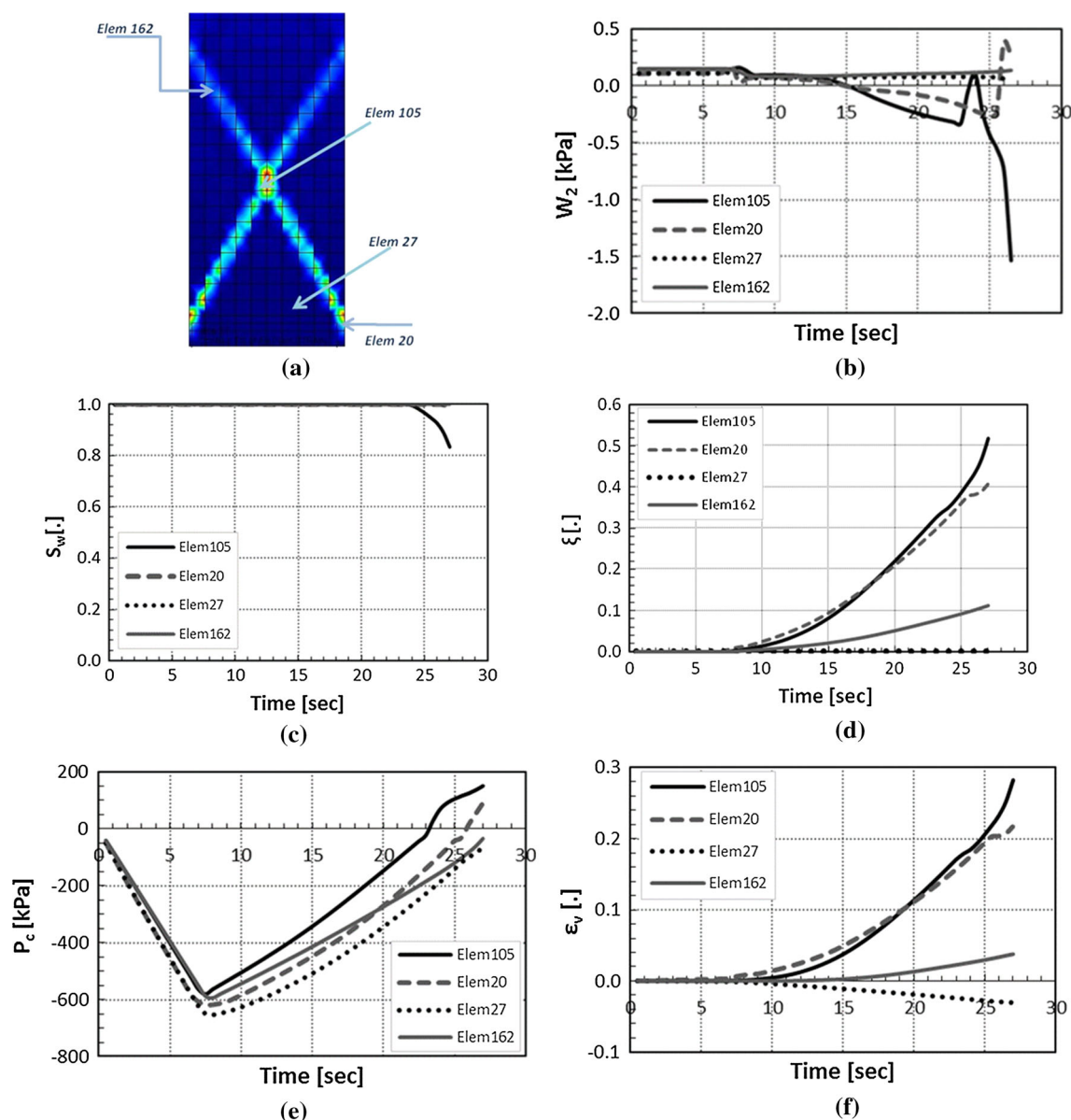
Fig. 6 a Material points location; b evolution of the W_2 (Eq. 14); c of the water saturation degree; d of the equivalent plastic strain; e of the capillary pressure; f of the volumetric strain, at these points

The values of the mechanical and hydraulic properties of each material layer which were used in the analysis are summarized in Table 2. These values were selected in agreement with [1, 44]. From the list of the material parameters, we can deduce that the pumice layers should be the first collapsible layers because of the lower value of cohesion in water-saturated condition and Young's modulus; they are also those with the higher permeability, and hence, the liquid water infiltrated with the rainfall and from the bedrock will penetrate easier and faster in the pumice layers, reducing their cohesion in unsaturated condition.

The rain gauges located at the toe of Pizzo d'Alvano massif recorded a cumulated rainfall value of more than

160 mm, for the period April 27–May 5, 1998. The daily rainfall for the analyzed period is shown in Fig. 10. However, according to [7], the cumulated rainfall must have been higher than the one measured at the toe, as the rain gauges which were installed at the top of the massif frequently gave higher values.

For the discretization of the geometry of the slope (Fig. 9), a rather coarse mesh has been used (Fig. 11), composed of 1565 nodes and 480 eight node quadrilateral isoparametric elements with a Gaussian integration of 3 x 3 order. In Fig. 11b, the elements at toe are presented as an example of the spatial discretization adopted in the computation; the size of these elements is variable in the range
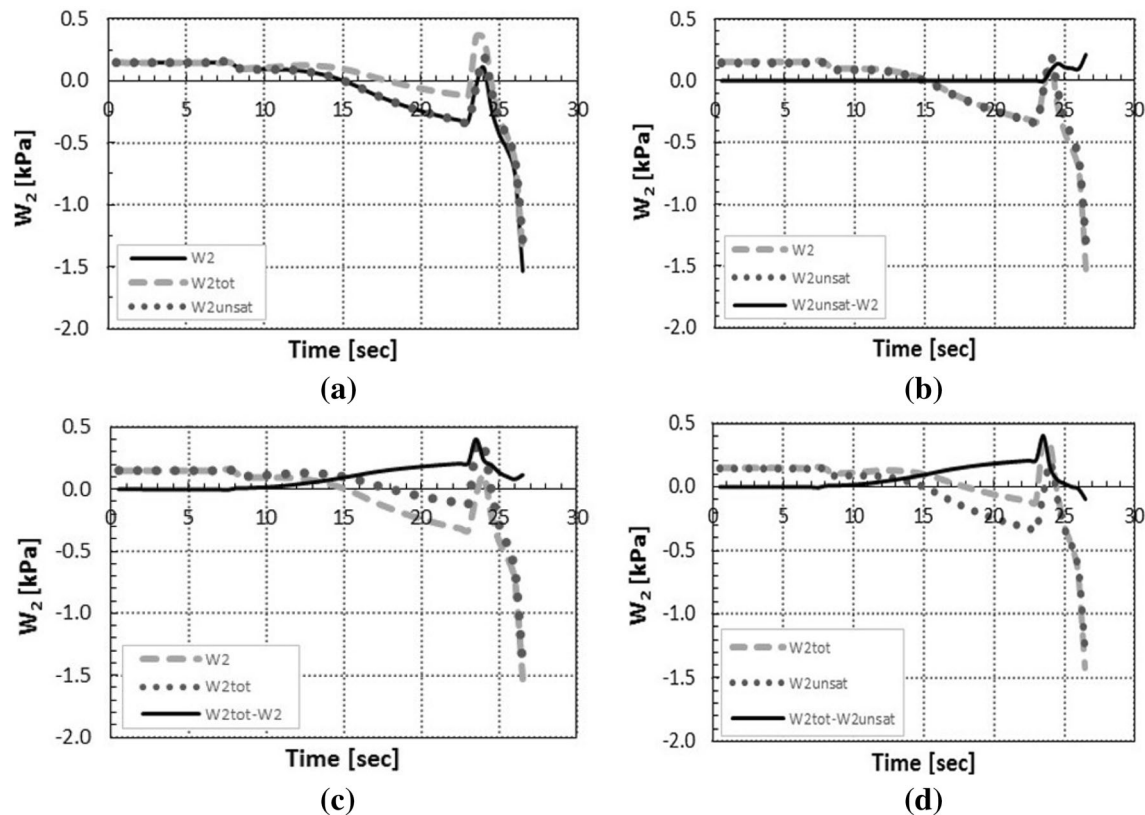
Fig. 7 a Comparison between the results obtained from the three different expressions of the second-order work (Eqs. 14, 15, 16) in the middle of the shear band; **b** evolution of the $W_{2unsat} - W_2$ difference; **c** evolution of the $W_{2tot} - W_2$ difference; **d** evolution of the $W_{2tot} - W_{2unsat}$ difference

0.11–0.34 m in height and about 9 m in length. This choice, with high aspect ratio, was made on the base of reducing the computational cost (min 2 h−max 52 h/day of rain) because the hydromechanical behavior (water flux and displacements) develops mainly along the axial direction (moreover, it is also observed that the numerical solution is convergent and consistent with the flowslides observed in situ, as described below in this section). When meshing the geometry of the stratigraphic section of Fig. 9, the toe of the slope was cut with a vertical side to avoid the generation of highly distorted finite elements in the toe region (see Fig. 11c).

Vertical and horizontal displacements are constrained at the bottom surface, which is also assumed impervious. The vertical boundary at toe of the discretized domain is not constrained to displacements, because it can move with the deformation of the slope, as can be seen in the Fig. 11c, and similarly, it is assumed impervious because the water flow at toe at the occurrence of the flowslide is unknown. This condition is realistic up to the saturation of the thickness of the slope at toe; then, when the condition of water saturation is reached, it overestimates the liquid water accumulation at toe and represents an upper bound for the numerical solution.

This choice can be reasonable as a first approximation and influences the numerical solution only during the 8th day of rain; during this period, the failure at toe of the slope was observed in situ. In fact, the numerical computation shows that: (1) the displacement of the vertical boundary at toe of the mesh remains very small and the behavior of the materials up to the first third of the 8th day of rain remains in the elastic regime (Fig. 18a); (2) the saturation of the thickness at toe occurs during the 8th day of rain (Fig. 19b) at which, simultaneously, the computed displacements increase continuously with high rate (Fig. 18a).

As a first step of the simulation, the stress state is computed in equilibrium with the gravity load, the boundary conditions and the initial hydrothermal conditions (Fig. 12), which, because of the low thickness of the slope, are a uniform capillary pressure of 10 kPa (reasonable value for the slope in the days before the rainfall, which were not rainy—see Fig. 10a), a uniform gas pressure at atmospheric value of 101.325 kPa and a uniform temperature at ambient value of 293.15 K.

After applying the rainfall load history, the results at the end of May 6 are presented below. In Fig. 13, it is observed that the displacements are mainly concentrated at the lower
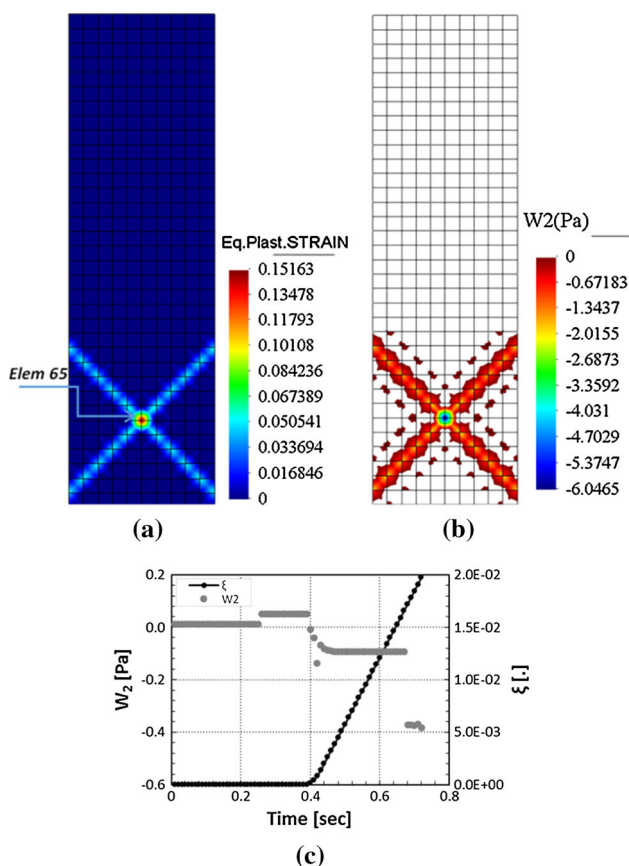
Fig. 8 Numerical results after 0.77 s of loading using the von Mises constitutive model: **a** equivalent plastic strain contour (.); **b** nil and negative values of the second-order work W_2 (Pa) contour; **c** evolution of the equivalent plastic strain and of W_2 in the middle of the shear band

part of the slope (near the toe, affecting a zone of 15 m length), with a maximum value of about 2 m.

The displacements are due to the accumulation of the plastic strain at the toe, as it is presented in the contour plot of the equivalent plastic strain variable on Fig. 14. In particular, as it was expected, the higher values are detected within the pumice layers which are the less resistant and the most permeable. The extent of the plastic zone and of the zone of displacements coincides with the zone of the increased degree of saturation, thus showing clearly the localized effect of the infiltrated water.

Apart from the localized effect at the lower portion of the slope, where the upslope groundwater flow is collected, the multiphase analysis reveals also the effect of the temporary spring from the bedrock observed after the event [6]. To this end, a flux condition was imposed at the basis of the pyroclastic deposits (Fig. 9, central part of the slope) with a volumetric inflow rate equal to 2.893 m^3/s from May 2.

The results presented in Figs. 15 and 16 at the end of May 5 highlight the important role of the local water circulation inside the bedrock showing, in particular, that the

area around the spring zone has been saturated (Fig. 16b) causing loss of soil strength and development of plastic strains at the base of the pyroclastic soils (Fig. 16a). This leads to the increase in the displacements (Fig. 15a, b), sliding and instabilizing of this zone (Fig. 16a, c, respectively) earlier than at the toe, as observed in situ during the flowslide events. These results are confirmed by the analysis of the W_2 value (Eq. 14) showing that the strongest indication of W_2 at the outlet occurs 5 h before the toe (the white regions in Fig. 16c represent zones with value of W_2 larger than $-1.0E-10$ Pa).

In order to understand better the main failure mechanism at the toe of the slope, we present hereafter the evolution of the above contour quantities in time, as this was captured on the different nodes (Fig. 17).

The calculated surface displacements, which are displayed in Fig. 18a, indicate a strong and continuous increase in nodal displacements during the 8th day of rain infiltration (May 6th) when the slope approaches failure. At the same time, large irreversible deformations occur at the toe of the slope with the largest values to be detected on the layers of the pumice (nodes 7, 15) as expected due to its low strength.

The contour of the equivalent plastic strain at the moment of failure is mainly due to the fact that by that time this zone has become fully saturated as it can be observed from the Fig. 19a. The evolution of the water table starts from the bottom on the 4th day (node 3) until it reaches the surface layers (nodes 19, 15) at the beginning of the 8th day.

This allows us to understand and analyze the mechanical response of the slope to rain infiltration: With increasing water content, the capillary forces acting between the soil particles decrease up to saturation of the pores (Fig. 19a) and pore water pressure develops (Fig. 19b). This de-bonding effect of wetting is taken into account in the model through the effective stress in the form $\boldsymbol{\sigma}' = \boldsymbol{\sigma} + [p^g - S^w p^c]\mathbf{1}$ [41], which decreases during rain infiltration, and as a consequence, the soil reduces its strength. When the point of significant excess pore water development is reached, there is little or no effective confining stress acting on the soil and the soil state may approach a zone of instability in which the shear strength decreases. Figure 20a, b describes this phenomenon in particular in the pumice layers (nodes 7 and 15), where it is observed that the capillary pressure (negative relative water pressure) vanishes up to the development of liquid water pressure (Fig. 19b); the mean pressure decreases down to zero and the deviatoric stress starts to decrease, suggesting a probable achievement of liquefaction (this state is then not described by the Drucker–Prager constitutive model adopted in this simulation because the loss of stiffness due to liquefaction is not modelled and the mean pressure starts to increase—Fig. 20a). This point would merit further
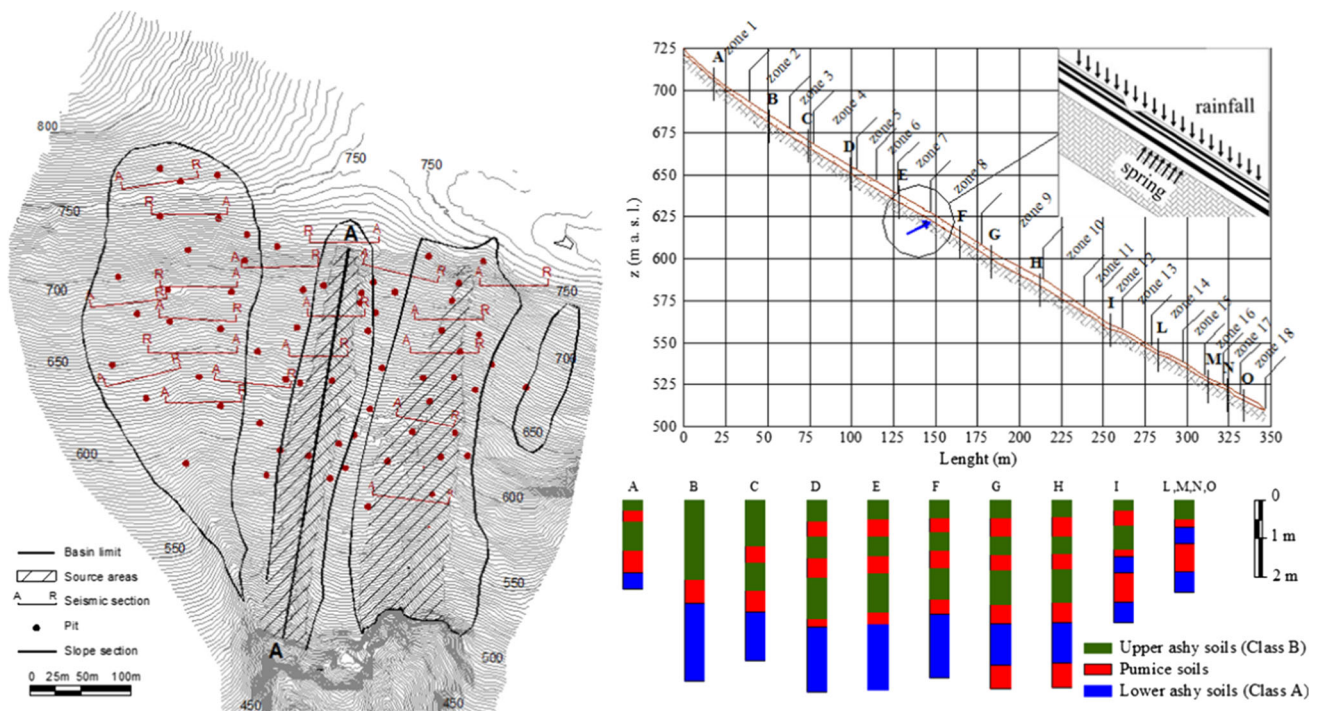
Fig. 9 Field site plan geometry and stratigraphy of the section A–A [7]

Table 2 Geotechnical characterization of soil layers

Definition	Label	Lower Ashy	Upper Ashy	Pumice
Solid grain density	ρ^s (kg/m^3)	2393	2169	2039
Young's modulus	E (Pa)	5E + 05	4E + 05	2E + 05
Poisson's ratio	v (–)	0.316	0.294	0.30
Friction angle	φ (°)	32.0	36.0	37.0
Friction angle associated with capillary pressure	φ^b (°)	25.0	25.0	25.0
Cohesion in water-saturated conditions	c (Pa)	4.7E + 03	4.7E + 03	**3.3E + 02**
Angle of dilatancy	ψ (°)	−4.75	−5.5	5
Softening modulus	h (Pa)	6.5E + 04	8.0E + 04	1.1E + 04
Hydraulic conductivity	k (m/s)	1E−06	1E−05	**1E−04**
Initial porosity	n (–)	0.664	0.584	0.69

investigation using a more advanced constitutive model able to describe the liquefaction state in soils both at stress and at stiffness level (e.g., the Pastor–Zienkiewicz model [35] and its extension to variably saturated conditions [2, 28]).

As far as the results of the second-order work W_2 are concerned, at the beginning of May 6 (8th day) we have the strongest indication of instability at the toe as shown in Fig. 21a. The negative values are concentrated in the pumice layers, at the upper ashy soil and at the base of the toe affecting a zone of about 21 m in length.

In Fig. 21b, c, the evolution of the second-order work W_2 (Eq. 14) is plotted in comparison with the evolution of the displacement rate and of the equivalent plastic strain at the material point level of the lower pumice layer (a gauss point of element 281, Fig. 21a, close to node 7 in the lower pumice layer, Fig. 17). It is observed that the second-order work W_2 becomes negative during the sharp increase in the displacement rate (Fig. 21b and zoom up in Fig. 21d) and the continuous development of plastic strain (Fig. 21c) and displacement (Fig. 18a). This behavior is observed also in other points, e.g., in a Gauss point at 4.5 m on the left of node 7. Few points of Fig. 21b, c deviate from the averaged interpolation line of the numerical results, but the general trend is not modified. It is observed also in the analysis of this section that the indication of the potential local instability from the W_2 comes later (difference of almost one day) than the beginning of plastic strains development,
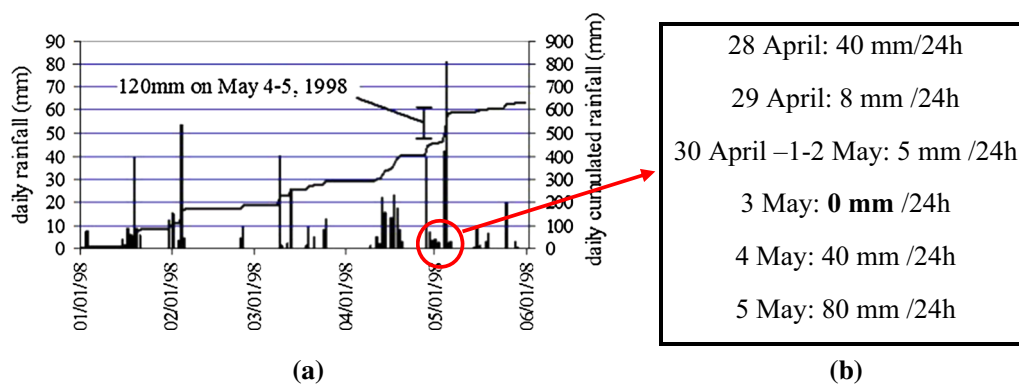
Fig. 10 a Rainfall recorded at the toe of Pizzo d'Alvano massif [7]; b rainfall loading function on the upper surface
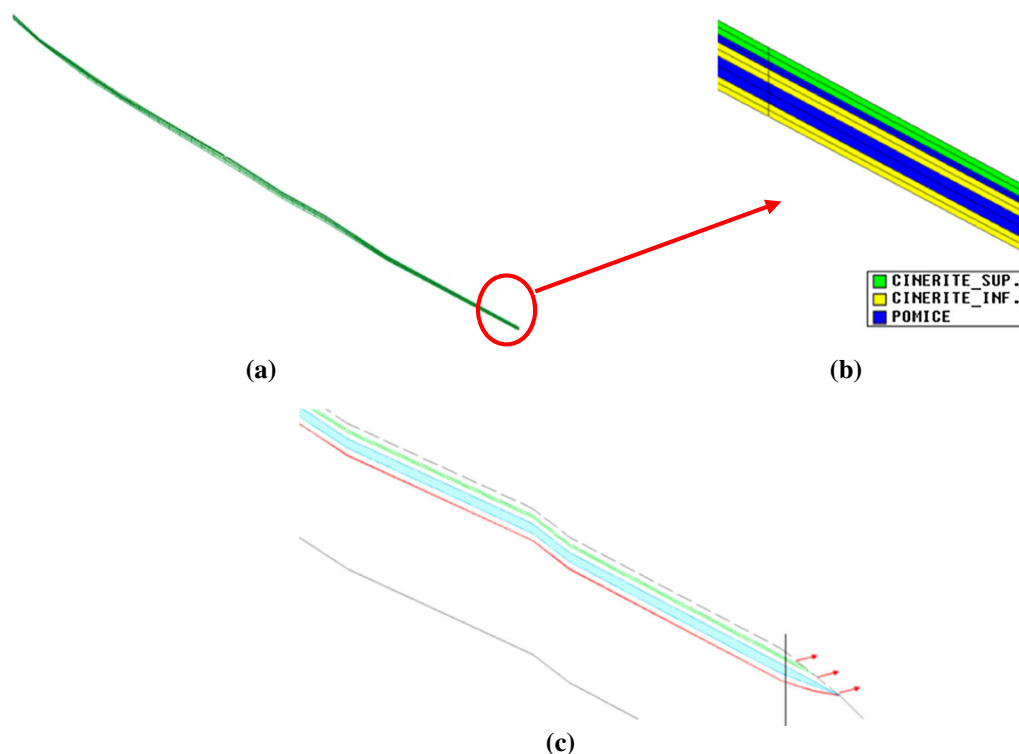

Fig. 11 a Discretization of the section A-A; b finite element discretization at the basis of the slope; c stratigraphic section of the slope at toe. The vertical line indicates the vertical boundary of the mesh at toe (Fig. 11b)

similarly to what is observed for the strain localization test. It can be also seen that the contour plot area of negative second-order work (Fig. 21a) coincides with that of the equivalent plastic strain at the toe of the slope (Fig. 14a) and the magnitude is greater than that corresponding to high displacements (Fig. 13a).

Finally, the numerical results of the second-order work W_{2tot} and W_{2unsat} as expressed from Eqs. (15) and (16), respectively, are presented in Fig. 22. When compared with the contour plot of the second-order work in terms of effective stress W_2 (Fig. 21a), it can be observed that the results of all the expressions are similar, especially for the

part of the slope which is saturated, with a greater extent for the W_{2unsat} variable (Fig. 22b). The comparison of the values between them shows that they are slightly different, with the expression of the second-order work accounting for the partially saturated conditions (W_{2unsat}) to give lower values.

7 Conclusion

In this work, the finite element modelling of two initial boundary value problems in geomechanics has been considered as a coupled variably saturated hydromechanical
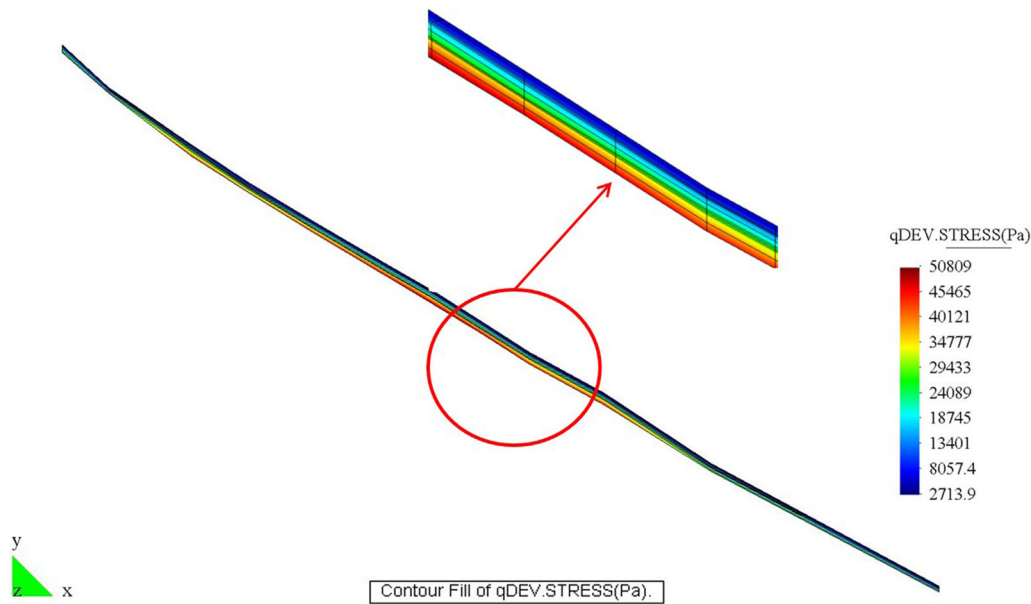
Fig. 12 Distribution of the deviatoric stress after the equilibrium with the initial and boundary hygro-thermal conditions
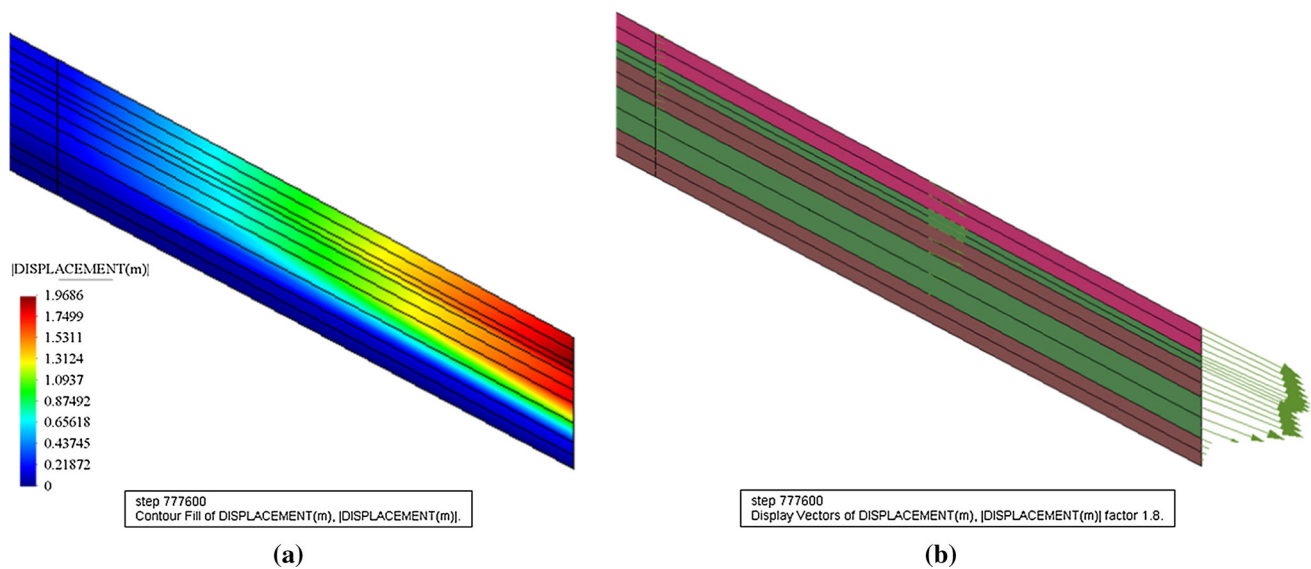

Fig. 13 **a** Displacement contour (m); **b** displacement vectors at the end of May 6 (lower part of the slope)

problem. Therefore, a multiphase model for elasto-plastic porous media has been used for the analyses, in conjunction with the second-order work criterion based on Hill's sufficient condition of stability. In particular, this modelling framework has been applied for the finite element analysis of plane strain compression tests of water-saturated dense sand and isochoric grain matter, where strain localization is observed, and of the failure initiation of a well-documented flowslide (Sarno-Quindici events, Italy, May 5–6, 1998).

The numerical results have pointed out that a sufficiently general coupled model for multiphase geomaterials is capable of modelling a variety of phenomena as strain localization in laboratory tests and the initiation of flow-slides, giving results in agreement with experimental or in situ observations, and can be a powerful tool for the understanding of the triggering mechanisms during the progressive localized or diffused failure (in the first case, a regularization procedure should be introduced for mesh objectivity upon mesh refinement, using, e.g., local or non-
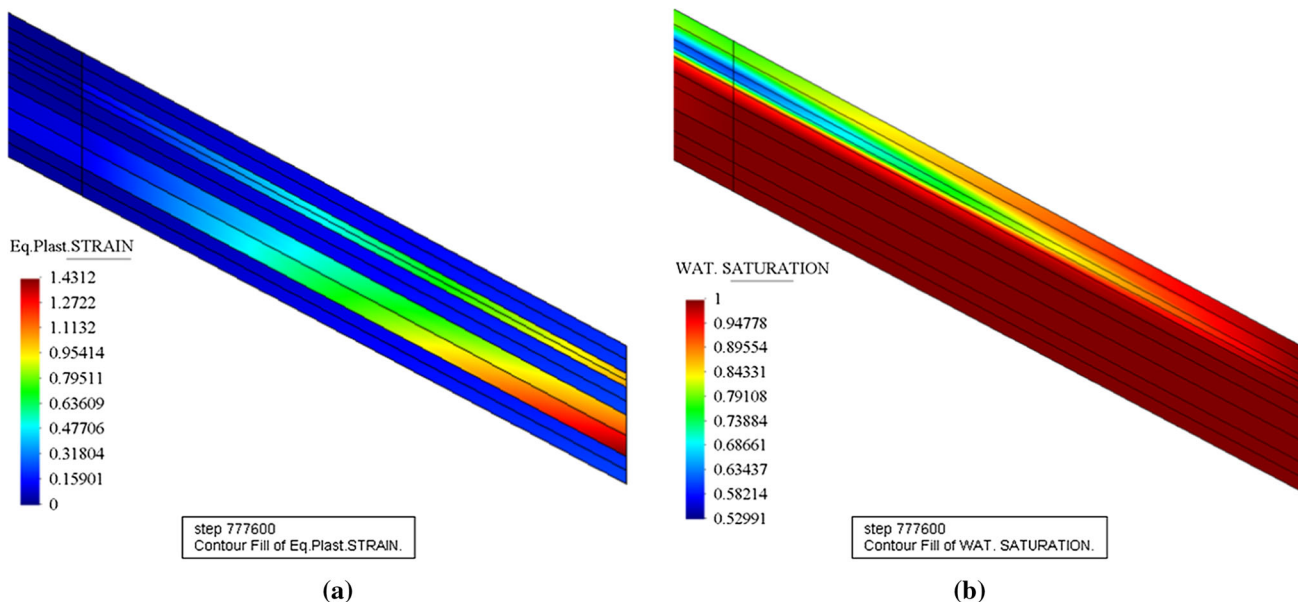
Fig. 14 **a** Equivalent plastic strain (–); **b** water saturation (–) contour at the end of May 6 (lower part of the slope)
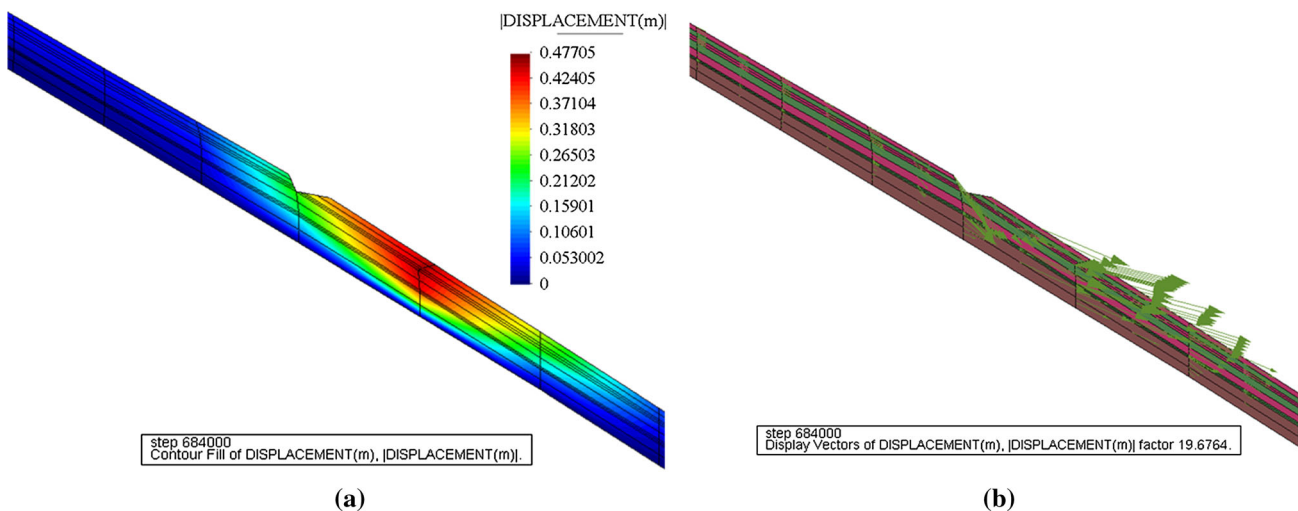

Fig. 15 **a** Displacement contour (m); **b** displacement vectors at the end of May 5 (spring zone)

local visco-plasticity as in [25], but this topic is beyond the scope of this work. In this paper, the width of the shear band has been fixed by the width of the finite element, with dimension similar to that of the experimental shear band).

What is more in this work is that the second-order work criterion, implemented in a finite element code for multiphase geomaterials (Comes-Geo, in our case), has been used in the simulations at the material point level to detect the zones with material point instability in the two cases mentioned above. Three different expressions have been presented, which could be used in case of variably saturated porous materials: the second-order work expressed in terms of effective stress, of total stress and thirdly by

taking into account the hydraulic energy contribution [4] for partially saturated soils.

The finite element results have shown that the set of the local negative values of the second-order work computed from the three expressions gives a good indication of the spatial extent of the potentially unstable domains and is consistent with the spatial and time evolution of variables that are adopted to detect the occurrence of localized or diffuse unstable zones as the equivalent plastic strain and the displacement and its rate; all expressions seem equivalent, but local values and also spatial extents are different, as expected, with a slightly better agreement for the expression of the second-order
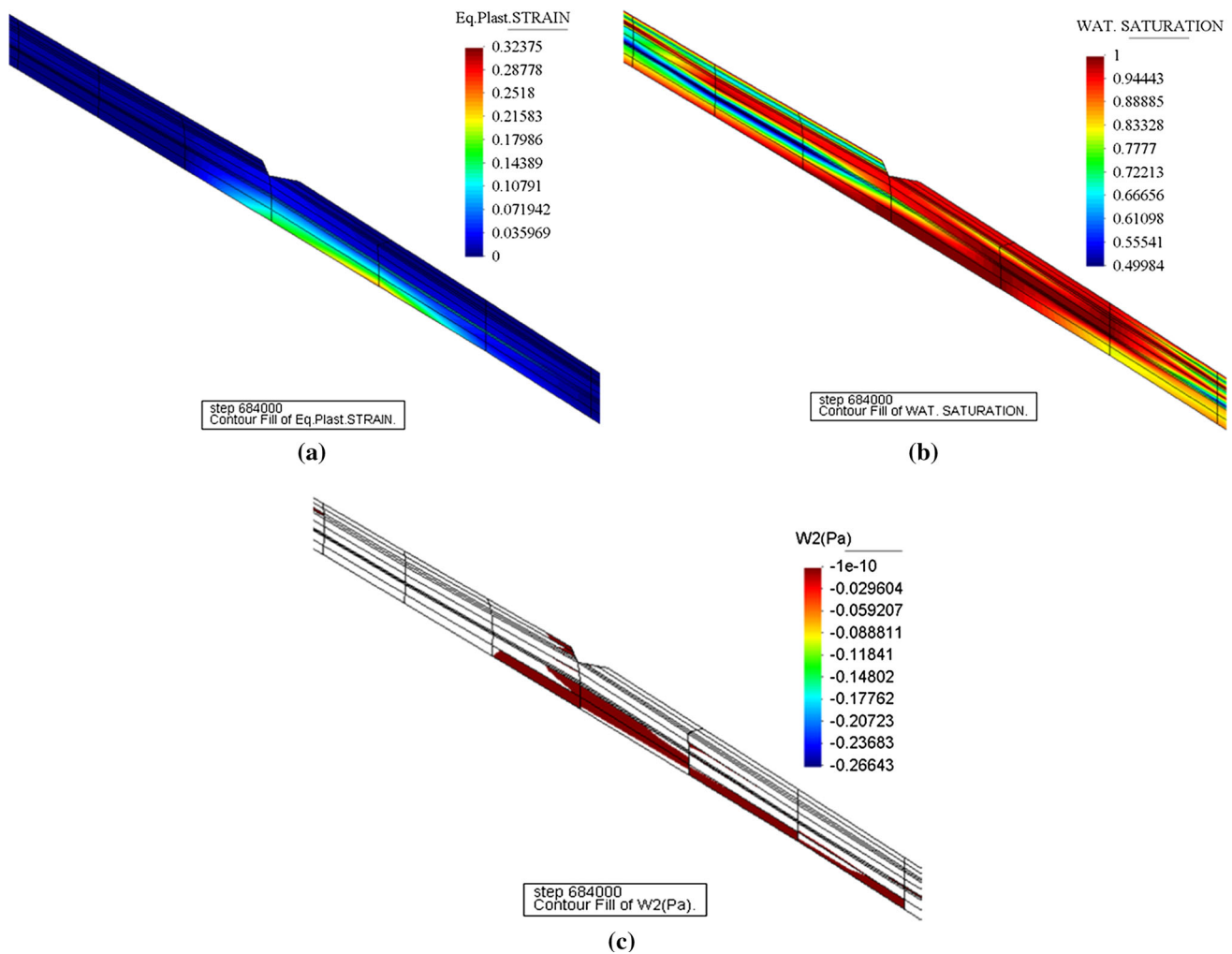
Fig. 16 **a** Equivalent plastic strain (−) contour; **b** water saturation (–) contour; **c** second-order work W_2 (Pa) contour at the end of May 5 (spring zone)
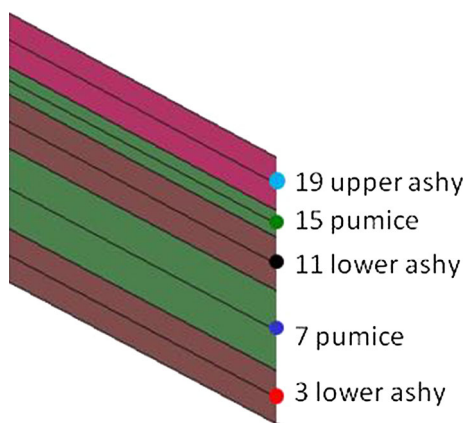

Fig. 17 Node location for the analysis at the lower part of the slope

work in terms of effective stress, W_2, and taking into account the hydraulic energy contribution, W_{2unsat}. The numerical results indicate also that the second-order work

criterion detects the local instability associated with cavitation of the pore water.

To extend these conclusions to the evaluation of the instability of the entire soil mass (the global domain), the value of the second-order work obtained by integration on the whole physical domain has to be computed. If this global value is negative, then entire domain is unstable [24, 27, 36] and the global value plays the role of a safety factor (see [36] in case of single phase material). When local negative values are obtained with a positive global value, the criterion indicates that the whole slope is still globally stable, possibly approaching to a properly unstable state; in this case, a limited zone with local negative values can indicate local instability and can also be an indication of a possible local failure mechanism.

Further research on this criterion is encouraged, in particular to investigate how this criterion can be related to the global instability and to combine the second-order work
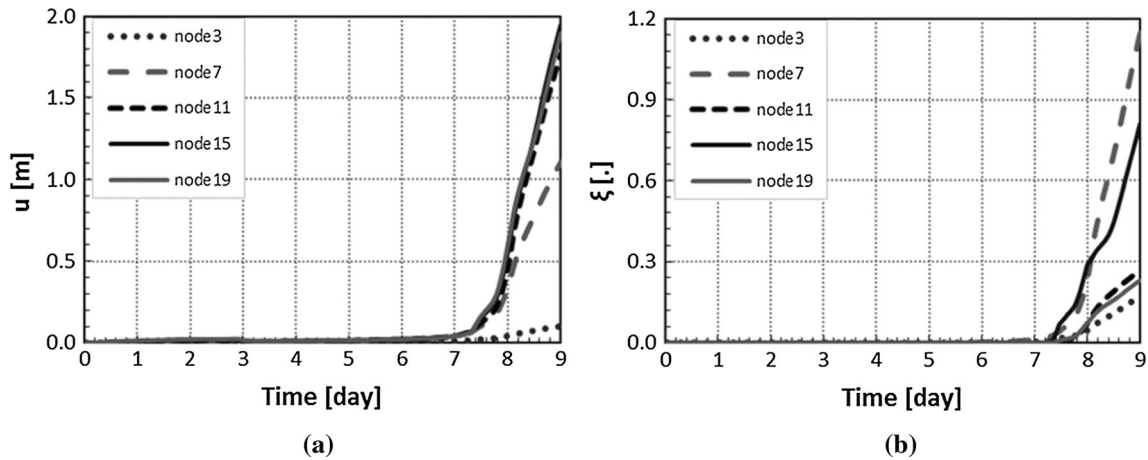
Fig. 18 **a** Evolution of the displacements (m); **b** the equivalent plastic strain (–) at the lower part of the slope
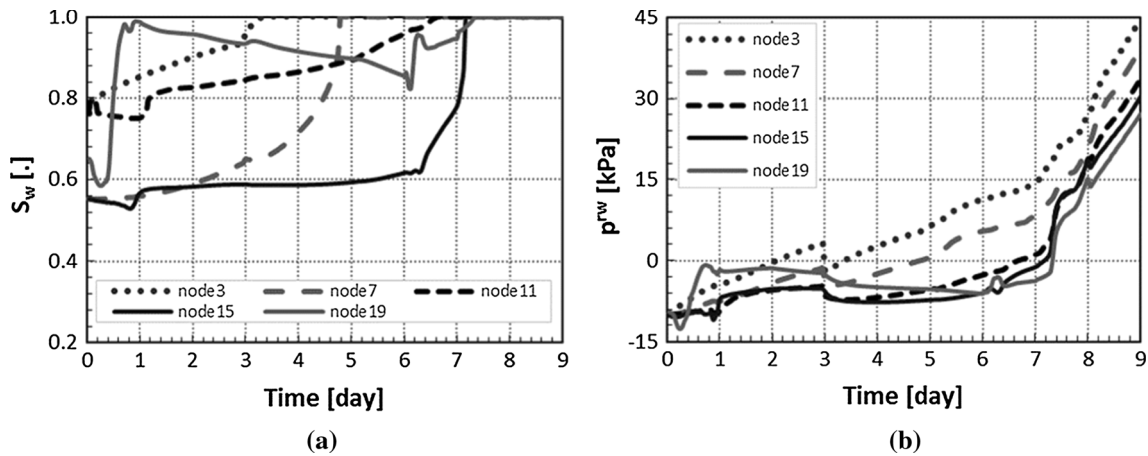

Fig. 19 **a** Evolution of the water saturation (–); **b** the relative water pressure (kPa) at the lower part of the slope
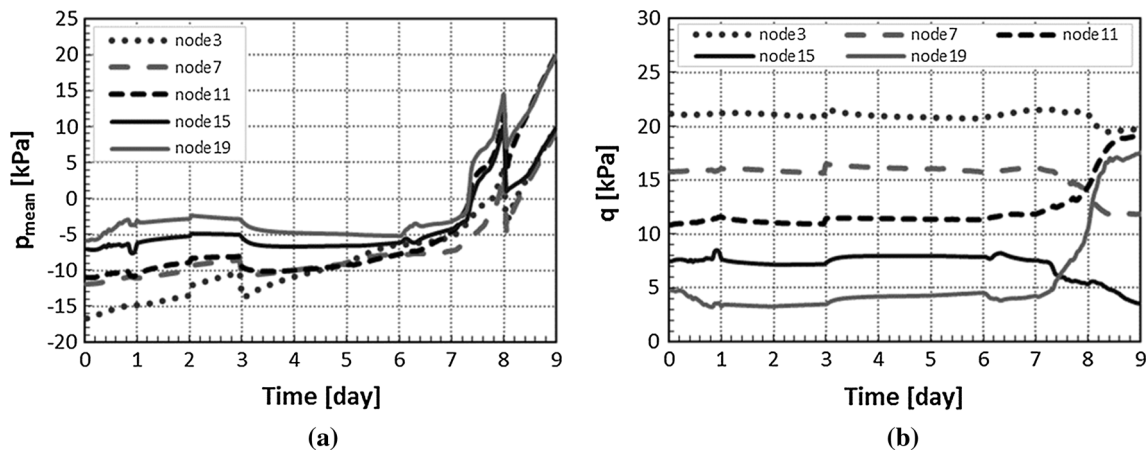

Fig. 20 **a** Evolution of the mean stress (kPa); **b** deviatoric stress (kPa) at the lower part of the slope

criterion with the results stemming from the bifurcation analysis for multiphase materials. This is necessary to evaluate separately the contribution of the hydro (capillary pressure/degree of saturation) and mechanical parts (stress/ strain). Also the use of advanced constitutive models for the solid skeleton is encouraged, to take into account the
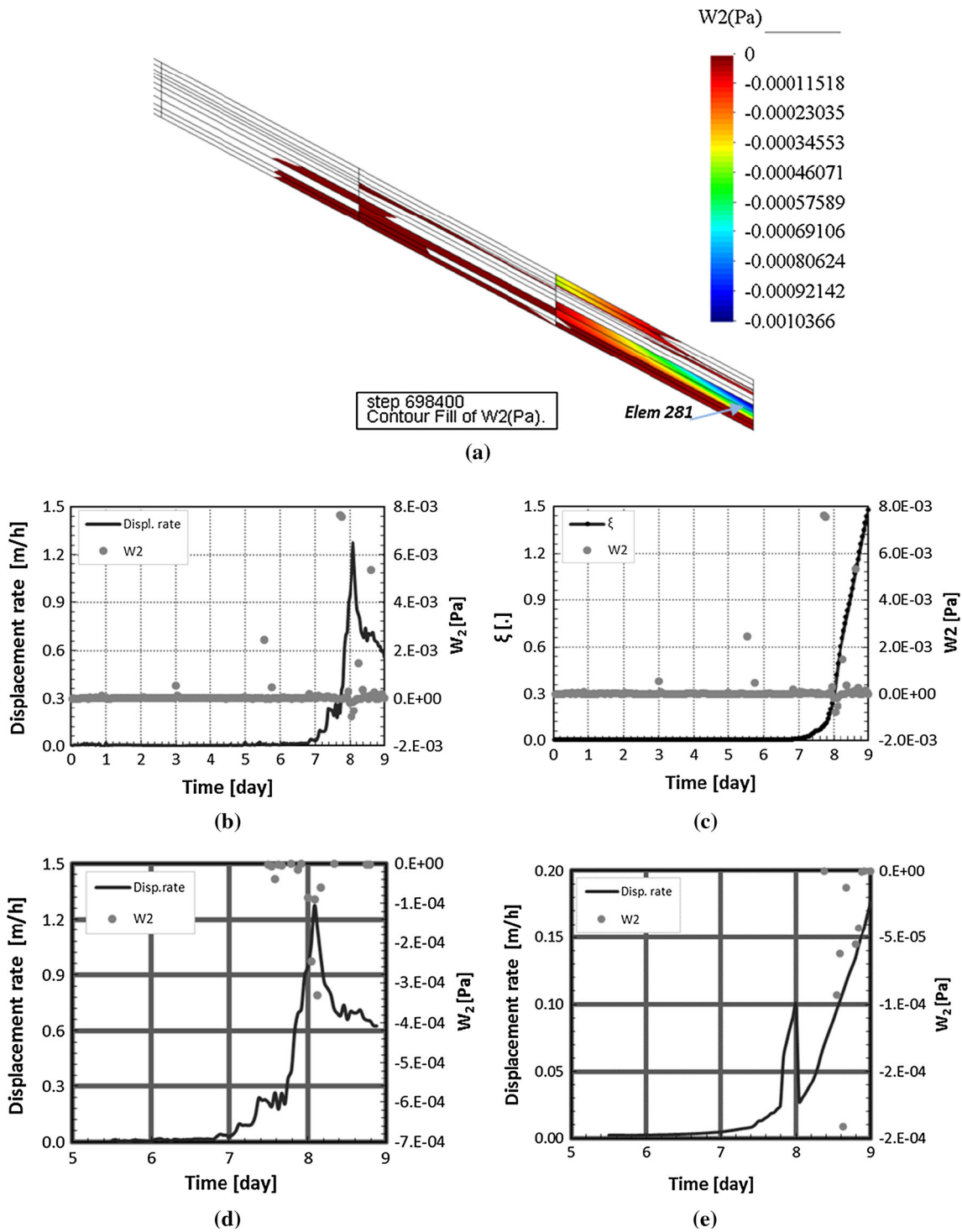
(a)

(b)

(c)

(d)

(e)

Fig. 21 **a** Second-order work contour in terms of effective stress at the beginning of May 6th (lower part of the slope); comparison between the evolution of the second-order work W_2 and the displacement rate **b**; and the equivalent plastic strain **c**, at the material point level in the lower pumice layer at toe. **d** Comparison between the evolution of the second-order work W_2 and the displacement rate for a Gauss point close to node 7—zoom up of Fig. 21b; **e** zoom up for a Gauss point at 4.5 m on the left of node 7 at the material point level in the lower pumice layer at toe
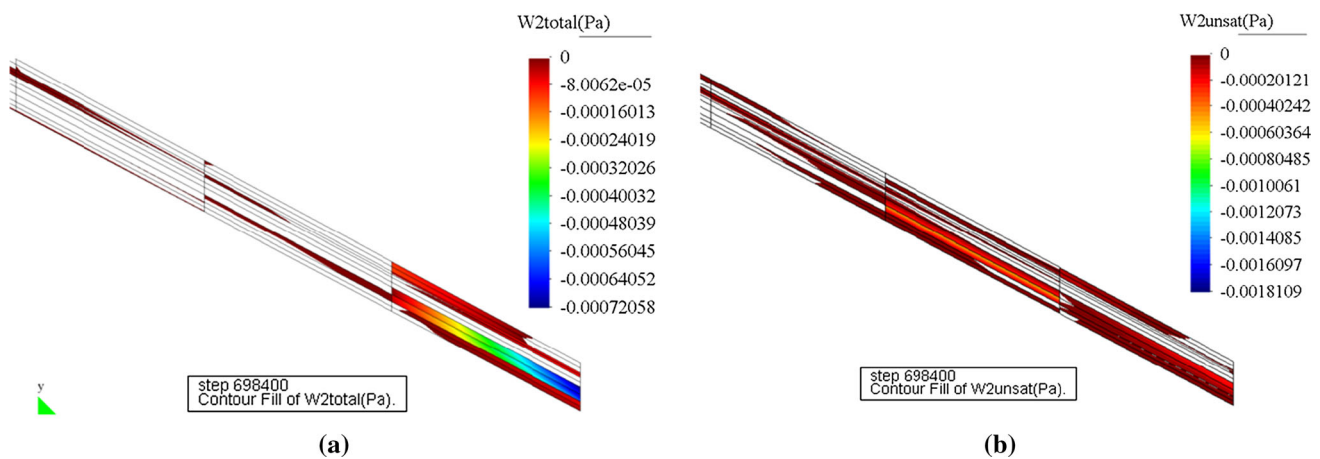
Fig. 22 Second-order work contour at the beginning of May 6th (lower part of the slope): **a** in terms total stress, W_{2tot}; **b** expression for partially saturated soils, W_{2unsat}

huge variety of the constitutive response of the geo materials.

Acknowledgments The authors wish to thank the 7th Framework Programme of the European Union (ITN MuMoLaDe project 289911) and the University of Padova (60A09-5709/14) for the financial support of this work.

References

1. Bilotta E, Cascini L, Foresta V, Sorbino G (2005) Geotechnical characterization of pyroclastic soils involved in huge flowslides. Geotech Geol Eng 23:365–402
2. Bolzon G, Schrefler B, Zienkiewicz O (1996) Elastoplastic soil constitutive laws generalized to partially saturated states. Géotechnique 46:279–289. doi:10.1680/geot.1996.46.2.279
3. Borja RI, White JA (2010) Continuum deformation and stability analyses of a steep hillside slope under rainfall infiltration. Acta Geotech 5:1–14. doi:10.1007/s11440-009-0108-1
4. Buscarnera G, Prisco C (2012) Discussing the definition of the second-order work for unsaturated soils. Int J Numer Anal Methods Geomech 36:36–49
5. Cascini L (2004) The flowslides of May 1998 in the Campania region, Italy: the scientific emergency management. Ital Geotech J 2:11–44
6. Cascini L, Guida D, Nocera N, et al. (2000) A preliminary model for the landslides of May 1998 in Campania Region. In: Picarelli E (ed) Proceedings 2nd international symposium geotech. Hard Soil- Soft Rock. Balkema, Napoli, pp 1623–1649
7. Cascini L, Sorbino G, Cuomo S (2003) Modelling of flowslides triggering in pyroclastic soils. In: Picarelli L (ed) Proceedings of international conference on "Fast Slope Movements—Predict Prev Risk Mitigation" Patron, Bologna, pp 93–100
8. Cascini L, Cuomo S, Sorbino G (2005) Flow-like mass movements in pyroclastic soils: remarks on the modelling of triggering mechanisms. Ital Geotech J 4:11–31
9. Cascini L, Cuomo S, Guida D (2008) Typical source areas of May 1998 flow-like mass movements in the Campania region, Southern Italy. Eng Geol 96:107–125
10. Cascini L, Cuomo S, Pastor M, Sorbino G (2010) Modeling of rainfall-induced shallow landslides of the flow-type. J Geotech Geoenviron Eng 136:85–98. doi:10.1061/(ASCE)GT.1943-5606.0000182
11. Daouadji A, Darve F, Al Gali H et al (2011) Diffuse failure in geomaterials : Experiments, theory and modelling. Int J Numer Anal Methods Geomech 35:1731–1773
12. Darve F (1994) Stability and uniqueness in geomaterials constitutive modelling. In: Chambon R, Desrues J, Vardoulakis I (eds) Localisation and bifurcation theory for soils and rocks. A.A. Balkema, Rotterdam, pp 73–88
13. Darve F, Servant G, Laouafa F, Khoa HDV (2004) Failure in geomaterials : continuous and discrete analyses. Comput Methods Appl Mech Eng 193:3057–3085. doi:10.1016/j.cma.2003.11.011
14. Fredlund DG, Morgenstern NR, Widger RA (1978) The shear strength of unsaturated soils. Can Geotech J 15:313–321
15. Gawin D, Schrefler BA (1996) Thermo-hydro-mechanical analysis of partially saturated. Eng Comput 13:113–143
16. Gray W, Hassanizadeh M (1991) Unsaturated flow theory including interfacial phenomena. Water Resour Res 27:1855–1863
17. Hassanizadeh M, Gray WG (1979) General conservation equations for multi-phase systems: 1. Averaging procedure. Adv Water Resour 2:131–144
18. Hassanizadeh M, Gray WG (1979) General conservation equations for multi-phase systems: 2. Mass, momenta, energy and entropy equations. Adv Water Resour 2:191–203
19. Hassanizadeh M, Gray WG (1980) General conservation equations for multi-phase systems: 3. Constitutive theory for porous media flow. Adv Water Resour 3:25–40
20. Hill R (1958) A general theory of uniqueness and stability in elastic-plastic solids. J Mech Phys Solids 6:239–249
21. Iverson RM (2000) Landslide triggering by rain infiltration. Water Resour Res 36:1897. doi:10.1029/2000WR900090
22. Iverson RM, Reid ME, LaHusen RG (1997) Debris-flow mobilization from landslides 1. Annu Rev Earth Planet Sci 25:85–138. doi:10.1146/annurev.earth.25.1.85
23. Laouafa F, Darve F (2002) Modelling of slope failure by a material instability mechanism. Comput Geotech 29:301–325
24. Laouafa F, Prunier F, Daouadji A et al (2011) Stability in geomechanics, experimental and numerical analyses. Int J Numer Anal Methods Geomech 35:112–139. doi:10.1002/nag.996

25. Lazari M, Sanavia L, Schrefler BA (2015) Local and non-local elasto-viscoplasticity in strain localization analysis of multiphase geomaterials. Int J Numer Anal Methods Geomech 39:1570–1592

26. Lewis RW, Schrefler BA (1998) The finite element method in the static and dynamic deformation and consolidation of porous media, 2nd edn. Wiley, Chichester, UK

27. Lignon S, Laouafa F, Prunier F et al (2009) Hydro-mechanical modelling of landslides with a material instability criterion. Géotechnique 59:513–524. doi:10.1680/geot.7.00121

28. Manzanal D, Pastor M, Merodo J (2011) Generalized plasticity state parameter-based model for saturated and unsaturated soils. Part II: Unsaturated soil modeling. Int J Numer Anal Methods Geomech 35:1899–1917

29. Mokni M, Desrues J (1998) Strain localisation measurements inundrained plane-strain biaxial tests on hostun RF sand. Mech Cohes Frict Mater 4:419–441

30. Nicot F, Darve F (2007) A micro-mechanical investigation of bifurcation in granular materials. Int J Solids Struct 44:6630–6652. doi:10.1016/j.ijsolstr.2007.03.002

31. Nicot F, Darve F (2011) Diffuse and localized failure modes: two competing mechanisms. Int J Numer Anal Meth Geomech 35:586–601

32. Nicot F, Darve F, Khoa HDV (2007) Bifurcation and second-order work in geomaterials. Int J Numer Anal Methods Geomech 31:1007–1032. doi:10.1002/nag.573

33. Nicot F, Daouadji A, Laouafa F (2011) Second-order work, kinetic energy and diffuse failure in granular materials. Granul Matter 13:19–28. doi:10.1007/s10035-010-0219-2

34. Nova R (1994) Controllability of the incremental response of soil specimens subjected to arbitrary loading programmes. J Mech Behav Mater 5:193–201

35. Pastor M, Zienkiewicz O, Chan A (1990) Generalized plasticity and the modelling of soil behaviour. Int J Numer Anal Methods Geomech 14:151–190

36. Prunier F, Chomette B, Brun M, Darve F (2016) Designing geotechnical structures with a proper stability criterion as a safety factor. Comput Geotech 71:98–114. doi:10.1016/j.compgeo.2015.09.007

37. Sanavia L (2009) Numerical modelling of a slope stability test by means of porous media mechanics. Eng Comput 26:245–266. doi:10.1108/02644400910943608

38. Sanavia L, Schrefler BA, Steinmann P (2002) A formulation for an unsaturated porous medium undergoing large inelastic strains. Comput Mech 28:137–151

39. Sanavia L, Pesavento F, Schrefler BA (2006) Finite element analysis of non-isothermal multiphase geomaterials with application to strain localization simulation. Comput Mech 37:331–348

40. Sanavia L, François B, Bortolotto R et al (2008) Finite element modelling of thermo-elasto-plastic water saturated porous materials. J Theor Appl Mech 38:7–24. http://www.imbm.bas.bg/tm/jtam/vol.38-1-2.php

41. Schrefler BA (1984) The finite element method in soil consolidation (with applications to surface subsidence). University College of Swansea

42. Schrefler BA (2002) Mechanics and thermodynamics of saturated/unsaturated porous materials and quantitative solutions. Appl Mech Rev 55:351–388

43. Sibille L, Hadda N, Nicot F et al (2015) Granular plasticity, a contribution from discrete mechanics. J Mech Phys Solids 75:119–139

44. Sorbino G, Foresta V (2002) Unsaturated hydraulic characteristics of pyroclastic soils. In: Proceedings of 3rd international conference on unsaturated soils. Swets and Zeitlinger, Lisse, pp 405–410

45. Swanson FJ, Swanston DN (1977) Complex mass-movement terrains in the western Cascade Range, Oregon. Rev Eng Geol 3:113–124

46. Zhang LL, Zhang LM, Tang WH (2005) Rainfall-induced slope failure considering variability of soil properties. Géotechnique 55:183–188